MIT Open Access Articles

Avoiding CO2 Improves Thermal Stability at the Interface of Li7La3Zr2O12 Electrolyte with Layered Oxide Cathodes

Avoiding CO₂ Improves Thermal Stability at the Interface of Li₇La₃Zr₂O₁₂ Electrolyte with Layered Oxide Cathodes

Younggyu Kim, Iradwikanari Waluyo, Adrian Hunt, and Bilge Yildiz*

Solid-state batteries promise higher energy densities and better safety than Li-ion batteries with liquid electrolytes. However, the interface between solid electrolyte and cathode is unstable at the elevated temperatures that are needed while sintering to achieve good bonding between ceramic components. Here, the hypothesis is that, the gas environment, especially the presence of CO₂, is critical in determining the stability of the solid electrolyte–cathode interface. The effect of gas species on the interface is systematically probed, by a using Li₇La₃Zr₂O₁₂ (LLZO) solid electrolyte with a thin film LiNi₀.₆Mn₀.₂Co₀.₂O₂ cathode as a model system to enable interface sensitivity. Detrimental phases formed at the interface and their onset conditions are identified by X-ray absorption spectroscopy, X-ray diffraction, and Gibbs free energy analysis. As a result, removing CO₂ and minimizing H₂O(g) during sintering is necessary to obtain good contact at the LLZO|cathode interface without forming secondary phases. Sintering in O₂ is ideal, yielding excellent chemical stability and low interfacial resistance. Secondary phases also do not form in N₂, but oxygen loss occurs at elevated temperatures. The interfacial resistance obtained upon sintering in pure O₂ is comparable to the lowest values at LLZO interfaces with protective coatings, but here without the need for interface coatings.

1. Introduction

All solid state Li-ion Batteries with nonflammable inorganic electrolytes are inherently safer than conventional batteries

Y. Kim, B. Yildiz
Laboratory for Electrochemical Interfaces
Department of Nuclear Science and Engineering
Massachusetts Institute of Technology
Cambridge, MA 02139, USA
E-mail: byildiz@mit.edu
Y. Kim, B. Yildiz
Department of Materials Science and Engineering
Massachusetts Institute of Technology
Cambridge, MA 02139, USA
I. Waluyo, A. Hunt
National Synchrotron Light Source II
Brookhaven National Laboratory
Upton, NY 11973, USA

(iD) The ORCID identification number(s) for the author(s) of this article can be found under https://doi.org/10.1002/aenm.202102741.

with flammable liquid electrolytes.[1] Li₇La₃Zr₂O₁₂(LLZO) is one of the most promising candidates among inorganic solid electrolytes because of its high ionic conductivity,[2] and electrochemical compatibility with Li metal anode.[3,4] The prospect of using a Li anode is especially compelling since it leads to much higher capacity compared to conventional lithium ion batteries using graphite anodes.[5] A critical bottleneck for developing successful solid-state batteries is minimizing the interfacial impedances between the solid electrolyte and the active electrode materials.[6–8] Despite challenges related to dendrite growth at Li|LLZO interfaces,[9,10] promising recent works led to improved interfacial stability by suppressing dendrite growth[11–14] and lowered interfacial resistance by improving the wetting at the Li|LLZO interface.[15–17]

However, the highest impedance generally exists at the electrolyte|cathode interface[6] and the instability at the LLZO-cathode interface remains an issue. Co-sintering process, which is needed to improve contact and bonding between ceramic cathode materials and the ceramic electrolyte LLZO, causes interdiffusion of elements and secondary phase formation,[18–22] with inferior transport properties.[7,23] Even though first-principles based computational predictions of reactivity between layered oxide cathode materials and LLZO predicted only low reactivity ($\Delta E_{reaction} \approx$ 1 meV per atom),[24] experimental results including those from our recent work showed that the interface degrades substantially through the formation of detrimental secondary phases. These detrimental secondary phases onset at rather moderate temperatures (300 to 500 °C), which are much lower than typical ceramic sintering conditions.[25–30] One reason for the discrepancy between the computational predictions and experimental results is the effect of the gas environment on the interface reactions, which was not taken into account in the computations.[7,23] Our earlier results have indicated the importance of the gas environment on the thermal stability of LLZO in contact with layered oxide cathode materials.[29,30] Li₂CO₃, LaCoO₃, and La₂Zr₂O₇ formed at the LiCoO₂ (LCO)|LLZO interface,[29] and Li₂CO₃, La(Ni,Co)O₃, and La₂Zr₂O₇ formed at LiNi₀.₆Mn₀.₂Co₀.₂O₂(NMC622)|LLZO[30] when these interfaces were annealed in air from 300 to 700 °C. Computational predictions, on the other hand, predicted the formation of Li-rich phases (Li₂NiO₃, Li₅CoO₄, and Li₂MnO₃).[24,31] In particular the presence of Li₂CO₃ as a reaction

product prompted us to hypothesize that CO_2 favors the formation of Li_2CO_3, and this leads to delithiating the LLZO, LCO, and NMC622, rendering these phases more unstable and more likely to react with each other, resulting in the formation of Li-deficient secondary phases. This warrants new experiments and calculations considering the gas environment explicitly when evaluating the stability of layered oxide cathode|LLZO interfaces, as we present in this paper.

It is well known that both bulk LLZO and layered oxide cathodes degrade by losing Li as they react with $H_2O(g)$ and $CO_2(g)$. LLZO degrades by forming LiOH and Li_2CO_3 near the surface under H_2O and CO_2 gas environment.[32,33] Layered oxide cathodes, especially the ones with high Ni content, also have similar stability issues with H_2O and CO_2.[34,35] Both LLZO and layered oxide cathodes become unstable by losing Li. LLZO decomposes into Li_2O_2, $Li_6Zr_2O_7$, La_2O_3, $La_2Zr_2O_7$, and O_2 upon delithiation.[36] Delithiated layered oxide cathodes transform to spinel and rock salt phases by losing oxygen.[37] Such instabilities due to Li-loss from LLZO and/or the layered oxide cathode can aggravate the thermodynamic instability between these phases at elevated temperatures. This is consistent also with the theoretical prediction that the reaction between delithiated LCO and LLZO is thermodynamically more favorable compared to the reaction between fully lithiated LCO and LLZO.[38]

Based on our earlier findings,[29,30] and the known detrimental role of $H_2O(g)$ and $CO_2(g)$ in destabilizing LLZO and layered oxide cathodes,[32–34] we believe it is important to assess the role of the gas environment in the stability of cathode|LLZO interfaces. In this work, we test this hypothesis by simple thermodynamic calculations and by model thin-film experiments with controlled gas environments. We used NMC622, which is a promising high voltage layered oxide cathode for experimental characterization. We used $LiCoO_2$ for thermodynamic calculations to predict and interpret qualitatively the reactivity between LLZO and a layered oxide cathode. LCO is simpler than NMC622 in deducing the reaction pathways and products, but yet representative given the presence of Co as a transition metal. We chose O_2, N_2, humidified O_2, and CO_2 gas environments to isolate their effect on the interfacial stability, as these constitute majority of gas species in air. Humidified O_2 and CO_2 environment were chosen to study the effect of $H_2O(g)$ and $CO_2(g)$ on interfacial degradation. O_2 and N_2 environments were control groups which don't contain $H_2O(g)$ and $CO_2(g)$.

Model systems comprising thin film cathode layers on LLZO pellets present advantages for studying interfacial degradation as demonstrated in our previous works.[29,30] The buried interface region of such thin films (≤100 nm) is within the detection depth of near-surface sensitive techniques such as soft X-ray absorption spectroscopy (XAS) using fluorescence yield detection mode. This allows us to detect the onset temperature of degradation and identify the phases without relying on destructive techniques such as transmission electron microscopy. Moreover, as XAS is sensitive to the oxidation state and local chemical environment, we could identify the onset of chemical reactions even when the formed phases had low crystallinity, unlike X-ray diffraction (XRD) on bulk powder samples whose sensitivity needs a large fraction of the sample to have degraded and formed high crystallinity.

Precise characterization of phase degradation and evaluation of their effect on charge transfer properties were possible by combining findings from XAS, XRD, and electrochemical impedance spectroscopy (EIS). Ruling out phases that did not match with XAS improved the reliability of our thin film XRD analysis.

As a result, pure O_2 gas condition was ideal, with good interface stability and decrease of interface resistance up to 700 °C. Sample annealed at 700 °C in O_2 had the lowest area specific resistance (ASR), 130 Ω·cm². This value is comparable to the lowest ASRs obtained at $LiCoO_2$|LLZO interfaces with coated interlayers.[39–42] In this work, by removing CO_2 from the gas environment during sintering, we succeeded in obtaining comparably low ASRs without the additional steps of depositing a protective interlayer.

To verify the relevance of the O_2-annealed interface, we have prepared and tested a Pt|NMC622|LLZO|Li cell, where the NMC622|LLZO was first annealed in O_2 at 500 °C. This sample had a first-charge capacity of 117 mAh g⁻¹, comparable to an earlier report on NMC622|LLZO all solid battery with a Li_3BO_3 interlayer,[43] and with the voltage plateaus for charging and discharging consistent with the lithiation and delithiation of NMC622. This result demonstrated that annealing the NMC622|LLZO in pure O_2 can indeed provide good initial electrochemical properties. Annealing in N_2 also led to a stable interface without any secondary phase formation. However, XAS revealed oxygen loss from NMC622. Even though the N_2 condition was less ideal than pure O_2, it could be a more cost-effective alternative compared to pure O_2 gas. Samples were hydrated after they were annealed in humidified O_2 at 500 °C, causing interface resistance increase. Upon further increase of annealing temperature in humidified O_2, NMC622 was dehydrated at 700 °C and had a lower interface resistance, comparable to that in pure O_2. This verified that the detrimental effect of humidity can be avoided if the annealing temperature is high enough. Finally, CO_2 environment was the most detrimental. Secondary phases formed at 500 and 700 °C, leading to a complete loss of the cathode|electrolyte capacitance. This comparison concludes that CO_2 is the key contributor for the interface degradation of NMC622|LLZO under thermal annealing conditions in ambient air.

These experimental results agree well with our thermodynamic predictions described above. The reaction between the cathode and the electrolyte was nonspontaneous ($\Delta G_{reaction} > 0$) for O_2 and N_2 environment, demonstrating that the interface should be stable in both gas conditions. The reaction was spontaneous at 300 °C ($\Delta G_{reaction} < 0$) and nonspontaneous at 700 °C ($\Delta G_{reaction} > 0$) in humidified environment, which is consistent with the experimental findings that the adverse effect of humidity can be reversed at high temperature. Finally, the reaction was spontaneous ($\Delta G_{reaction} < 0$) for pure CO_2 at 300 to 700 °C, which is consistent with the major degradation found in CO_2 environment.

Our findings demonstrate the importance of controlling the gas environment during the sintering process to obtain good contact between the ceramic cathode and ceramic electrolyte in solid state batteries. Co-sintering the cathode and electrolyte in O_2 environment gives chemically stable interface with low interfacial resistance.

2. Experimental Design and Methods

We prepared samples for XAS and XRD by depositing 100 nm thin dense NMC622 layers on top of polished LLZO pellets by RF sputtering at ambient temperature. This thickness allows for sensitivity to the buried interface while measuring the

transition metal L-edge spectrum XAS.[30] Annealing conditions were 300, 500, and 700 °C for 4 h in different gas environments, including pure O_2, pure N_2, humidified O_2 (2 wt% H_2O in O_2), and pure CO_2 at 1 atm. We prepared the humidified O_2 (2 wt% H_2O in O_2) environment by flowing O_2 through a gas bubbler at room temperature. Temperature range used for annealing in this work includes crystallization temperatures for deposited layered oxide cathode thin films.[44–47]
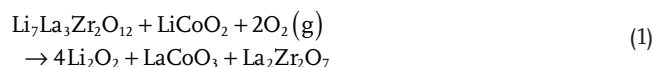
We prepared symmetric cells for EIS characterization by depositing 60 nm NMC622 on both sides of polished LLZO pellets, and with 60 nm Au on NMC622 for current collection. Annealing of the samples in the same conditions as described above were done prior to Au deposition. Since these symmetric cells do not have an anode|electrolyte interface, the change in the EIS was only a result of changes at the cathode|electrolyte interfaces. We worked with a thicker NMC622 layer, 370 nm, with ¼″ diameter, for electrochemical cycling experiment. After annealing the NMC622|LLZO at 500 °C for 4 h in O_2, we deposited 200 nm Pt current collector on top of NMC622 film. We used a 5/16″ diameter Li metal foil anode, pressed onto the polished LLZO pellet in the glovebox. Annealing condition for Li attachment was 160 °C, 30 min. Polishing, annealing and pressing lowers the LLZO|Li interfacial resistance and gives stable overpotential at the interface during cycling.[17,32]
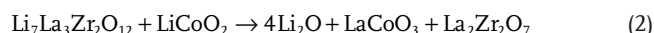
3. Results

3.1. Thermodynamic Calculations of Interfacial Degradation

We used $LiCoO_2$ for thermodynamic calculation of the Gibbs free energy to predict and interpret qualitatively the reactivity between LLZO and a layered oxide cathode. LCO is simpler than NMC622 in deducing the reaction pathways and products, but yet representative as a layered transition metal oxide. In our earlier work, we have found that $LiCoO_2$|LLZO interface decomposes by forming Li deficient phases ($LaCoO_3$, $La_2Zr_2O_7$) and a Li-sink (Li_2CO_3) upon thermal annealing in air.[29] Based on this finding, we propose that the following reactions between $LiCoO_2$ and LLZO in different gas conditions include a Li-sink and Li-deficient phases:
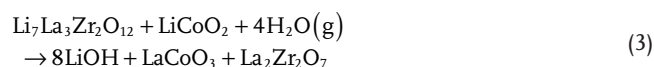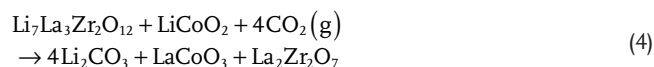
a) Pure O_2 environment:

$$Li_7La_3Zr_2O_{12} + LiCoO_2 + 2O_2(g) \rightarrow 4Li_2O_2 + LaCoO_3 + La_2Zr_2O_7 \tag{1}$$

b) Inert environment:

$$Li_7La_3Zr_2O_{12} + LiCoO_2 \rightarrow 4Li_2O + LaCoO_3 + La_2Zr_2O_7 \tag{2}$$

c) Humidified environment:

$$Li_7La_3Zr_2O_{12} + LiCoO_2 + 4H_2O(g) \rightarrow 8LiOH + LaCoO_3 + La_2Zr_2O_7 \tag{3}$$

d) CO_2 environment:

$$Li_7La_3Zr_2O_{12} + LiCoO_2 + 4CO_2(g) \rightarrow 4Li_2CO_3 + LaCoO_3 + La_2Zr_2O_7 \tag{4}$$

Figure 1 shows the Gibbs free energy, $\Delta G(T,P_{gas})$ (in units of kJ mol^{-1} of LLZO), of these reactions for each gas environment. Details for the $\Delta G(T,P_{gas})$ calculations are in Experimental Section. The pressure and temperature ranges for these calculations are 10^{-5} bar to 1.01325 bar (1 atm), and 300 to 700 °C, respectively.

The calculated reaction energies $\Delta G(T,P_{gas})$ indicate stable cathode|electrolyte interface when the sample is annealed in O_2 and in inert environment. Reactions in those two gas environments were always nonspontaneous in the temperature and pressure ranges in Figure 1a,b. In contrast, $\Delta G(T,P_{gas})$ for the reaction including $H_2O(g)$ was negative (spontaneous) below 449 °C and positive (nonspontaneous) over 449 °C for humidified O_2 (2 wt% H_2O in O_2) (Figure 1c). CO_2 was the most detrimental gas environment. $\Delta G(T,P_{gas})$ for CO_2 environment was the most negative when compared to $\Delta G(T,P_{gas})$ values for other environments at same pressure and temperature conditions (Figure 1d). Moreover, ΔG was always negative for 1 atm CO_2 at 300 °C to 700 °C. Therefore, these thermodynamic calculations predict interfacial degradation upon annealing in CO_2 environment.
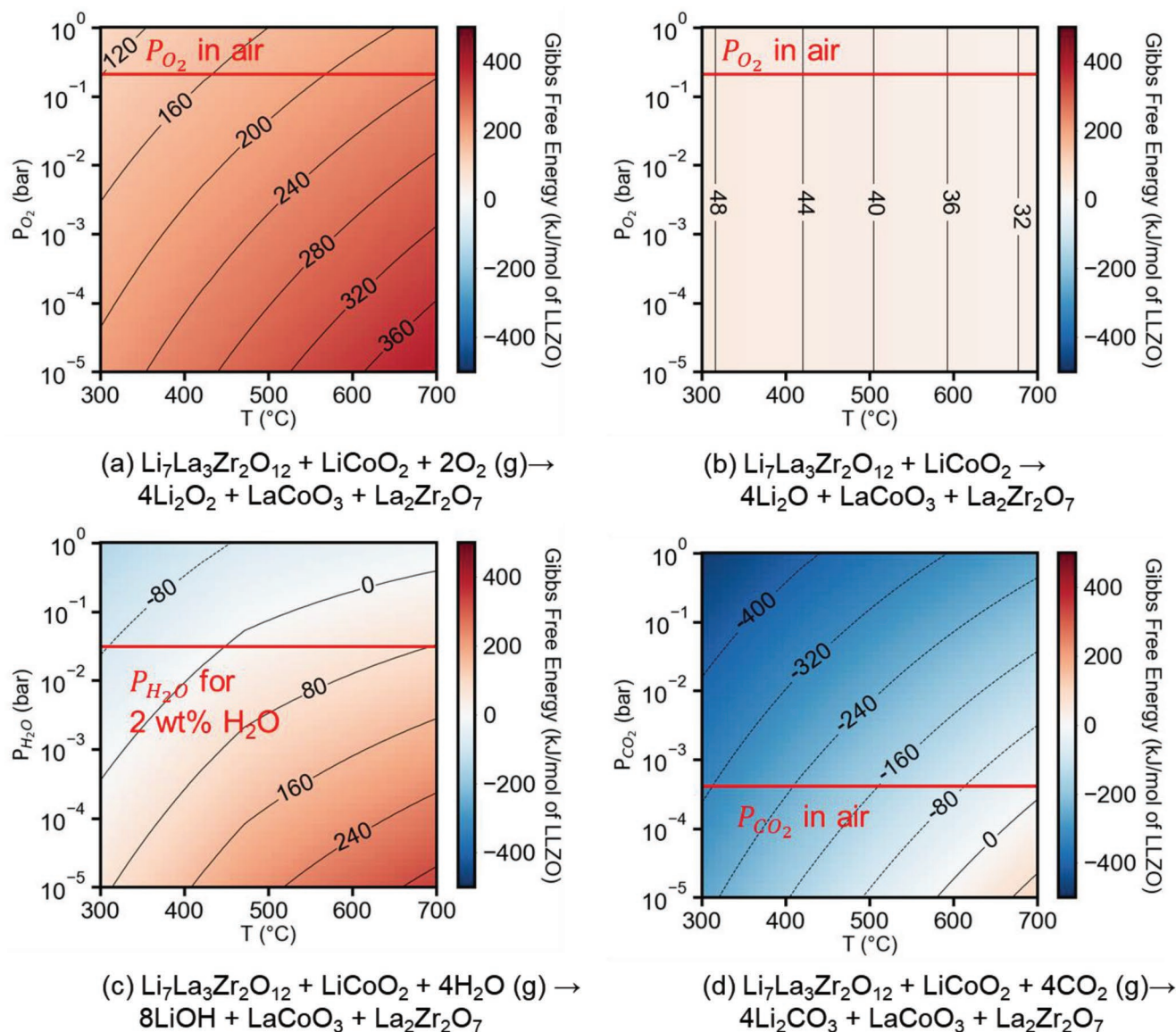
3.2. Oxidation State and Local Chemical Environment Analyzed by Soft X-Ray Absorption Spectroscopy

We investigated O K-edge, Ni $L_{2,3}$-edge, La $M_{4,5}$-edge, and Co $L_{2,3}$-edge of the NMC622|LLZO samples annealed in different gas environments. **Figure 2** shows O K-edge spectra. The pre-edge feature (528–532 eV) corresponds to electronic transition from the oxygen 1s orbital to the oxygen 2p orbital that is hybridized with the transition metal 3d orbitals.[48] Neither LLZO nor Li_2CO_3 has features in this energy range.[28,29,49] Therefore, any change in this O K pre-edge feature is only dependent on the change of the oxygen-transition metal bonds in the system. Broad features around 542 eV correspond to electronic transition to hybridized states between oxygen 2p orbital and transition metal 4s, 4p orbitals.[48]

The intensity of the pre-edge feature increased up to 500 °C and decreased at 700 °C for samples annealed in O_2 (Figure 2a). The pre-edge intensity growth originates from the increase of coordination number of transition metals with oxygen due to oxidation of the sample. Decrease of the pre-edge feature at 700 °C shows that there exists some degree of chemical evolution even in O_2 environment, but it is not as severe as other gas environment (N_2, humidified O_2, CO_2) as seen in Figure 2b–d.

The pre-edge feature intensity decreased as annealing temperature increased for samples annealed in N_2 (Figure 2b). Especially, the intensity of the pre-edge feature at 700 °C dropped considerably compared to the as-deposited sample. The trend originates from the decrease of coordination number of transition metals with oxygen due to oxygen loss in N_2 environment. The result matches well with works by Guo et al.,[50] and Zhong et al.[51] on oxides with transition metal-oxygen bonds. O K pre-edge intensity decreased as the number of oxygen vacancies increased in both studies.[50,51]

Pre-edge intensity for the sample annealed in humidified O_2 was highest at 500 °C. Data from the sample annealed at 500 °C stood out since pre-edge intensity for the other temperature

2102741 (3 of 18)

**ADVANCED
SCIENCE NEWS**

www.advancedsciencenews.com

**ADVANCED
ENERGY
MATERIALS**

www.advenergymat.de

Figure 1. The Gibbs free energy, $\Delta G(T,P_{gas})$ (kJ mol^{-1} of LLZO) calculated between LLZO and fully lithiated $LiCoO_2$ in a) $Li_7La_3Zr_2O_{12} + LiCoO_2 + 2O_2(g) \rightarrow 4Li_2O_2 + LaCoO_3 + La_2Zr_2O_7$, b) $Li_7La_3Zr_2O_{12} + LiCoO_2 \rightarrow 4Li_2O + LaCoO_3 + La_2Zr_2O_7$, c) $Li_7La_3Zr_2O_{12} + LiCoO_2 + 4H_2O(g) \rightarrow 8LiOH + LaCoO_3 + La_2Zr_2O_7$, and d) $Li_7La_3Zr_2O_{12} + LiCoO_2 + 4CO_2(g) \rightarrow 4Li_2CO_3 + LaCoO_3 + La_2Zr_2O_7$.

conditions in humidified O_2 decreased as annealing temperature increased. Moreover, post-edge features around 542 eV were much broader than the spectra obtained from other temperature conditions.

Hydration of NMC622 at 500 °C explains findings from the O K-edge analysis. Hydration of $LiNiO_2$, which has the same crystal structure as NMC622, happens by Li$^+$/H$^+$ substitution.[52,53] Moshtev et al., suggested that γ-NiOOH, which is isostructural to $LiNiO_2$, forms by Li$^+$/H$^+$ substitution in $LiNiO_2$,[54] Pritzl et al.,[55] and Jeong et al.[56] also claimed phase transformation from layered oxide to M-OOH(M:Ni,Co) like structure by hydration. Especially, Jeong et al., observed formation of CoOOH at the surface of hydrated $LiCoO_2$ with XPS.[56]

γ-NiOOH O K-edge EELS spectra had a stronger pre-edge feature and a broader post-edge feature compared to $LiNiO_2$,[57]

which agrees with our finding (Figure 2c). In our case, hydration led to the formation of γ-NiOOH local chemical environment, rather than full transformation to crystallized γ-NiOOH phase since the corresponding peaks could not be seen from XRD data. Since XAS depends on local chemical environment, this is sufficient for identifying the identity of the compound from the XAS spectra in Figure 2c.

Pre-edge intensity decreased as annealing temperature increased for samples annealed in CO_2 (Figure 2d). Notably, the pre-edge feature for NMC622 completely disappeared at 700 °C. O K-edge spectral shape matched well with Li_2CO_3.[58] Since the typical detection depth of PFY is ≈100 nm,[59] more than 100 nm Li_2CO_3 has grown on the surface during annealing.

Figure 3 shows XAS spectra for La $M_{4,5}$-edge and Ni $L_{2,3}$-edge. We normalized data by La M_5-edge to compare the magnitude
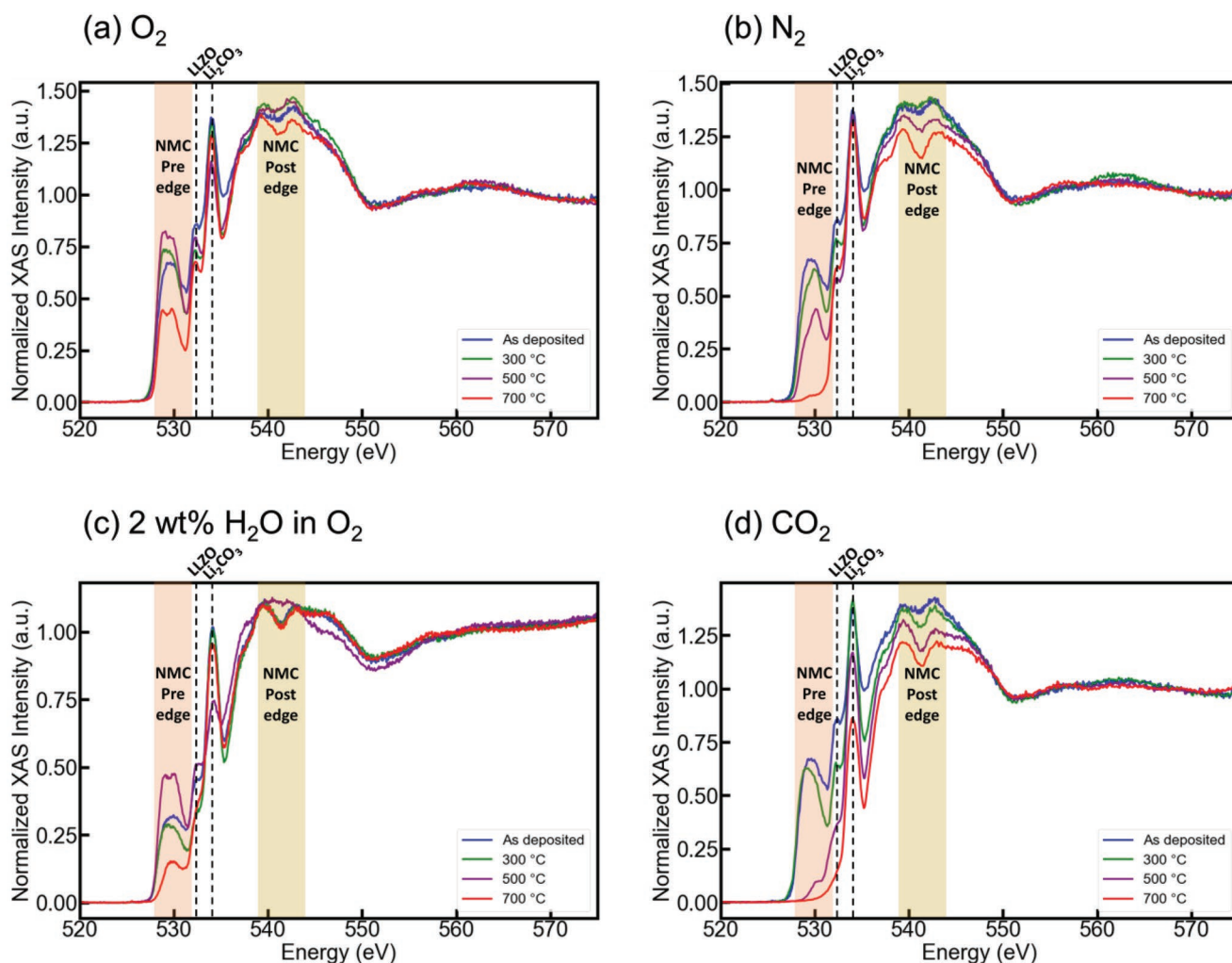
Figure 2. O K-edge X-ray absorption spectra measured by partial fluorescence yield (PFY) mode for 100 nm NMC622|LLZO. Spectra for the as-deposited sample and the samples annealed in a) O_2, b) N_2, c) 2 wt% H_2O in O_2, and d) CO_2 at 300–700 °C for 4 h are shown.

of Ni $L_{2,3}$-edge for each sample as we assume La oxidation state does not change. L-edge originates from 2p to 3d electronic transition,[60] so the intensity of the Ni L-edge depends on both quantity of Ni in the detection regime and number of holes in 3d orbitals. Therefore, Figure 3 gives not only the elemental ratio of Ni/La within the detection depth, but also the electronic configuration in each Ni 3d orbitals.
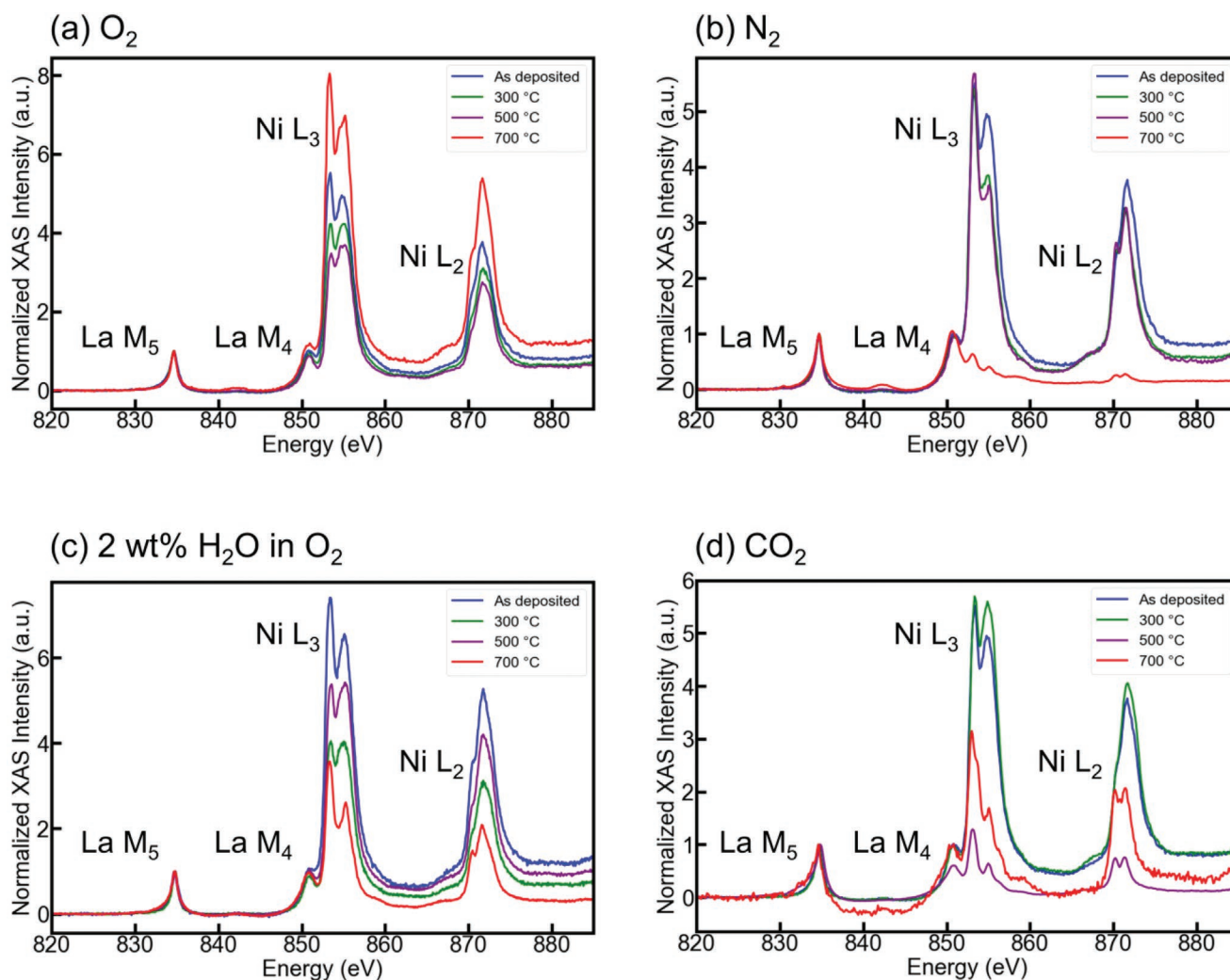
Ni L-edge intensity decreased up to 500 °C for samples annealed in O_2, likely due to migration of Ni through NMC622|LLZO interface (Figure 3a). Interestingly, Ni L-edge intensity increased at 700 °C. The behavior could originate from the increase of number of Ni-O bonds due to annealing in O_2 environment. This can be due to both increased oxidation state and increased crystalline order, along with changes in electronic structure, compared to the films that were sputter-deposited at room temperature. This led to more electrons transferred from Ni 3d orbitals to O 2p orbitals, causing increase of L-edge intensity.[61]

Ni L-edge intensity decreased as annealing temperature increased for samples annealed in N_2 (Figure 3b). Notably, Ni L-edge intensity decreased steeply at 700 °C because of oxygen

loss, as the sample was annealed in reducing environment. Oxygen loss led to more electrons localized in Ni 3d orbitals, and decrease of L-edge intensity. If the behavior at 700 °C was due to Ni migration, evidences for secondary phase formation from Co L-edge XAS or XRD should also be seen considering our former study on NMC622|LLZO interfacial degradation.[30] However, those indicators were not found.

Ni L-edge intensity decreased as annealing temperature increased in humidified O_2, except the sample annealed at 500 °C (Figure 3c). Formation of γNiOOH like local environment explains high L-edge intensity found at 500 °C, which we noted during O K-edge analysis. Oxidation state of Ni in γNiOOH is 3.48–3.68.[62] Therefore, it explains increase of Ni L-edge intensity due to increase of number of holes in 3d orbital.

Moreover, Ni got reduced at 700 °C in humidified O_2 (**Figure 4**). The low energy shoulder of the Ni L_2 edge grew and the peak shifted toward lower energy at 700 °C, which indicated reduction.[20,63,64] This comes from dehydration of the sample at 700 °C after hydration during temperature ramp up. Similar to NiOOH which decomposes to NiO, O_2, and H_2O at high

ADVANCED
SCIENCE NEWS

www.advancedsciencenews.com

ADVANCED
ENERGY
MATERIALS

www.advenergymat.de

Figure 3. La M_5, La M_4, Ni L_3, and Ni L_2 X-ray absorption spectra measured by partial fluorescence yield (PFY) mode for 100 nm NMC622|LLZO samples. Spectra for as deposited sample and sample annealed in a) O_2, b) N_2, c) 2 wt% H_2O in O_2, and d) CO_2 for 4 h are shown. Intensities of peaks were normalized by La M_5 edge.
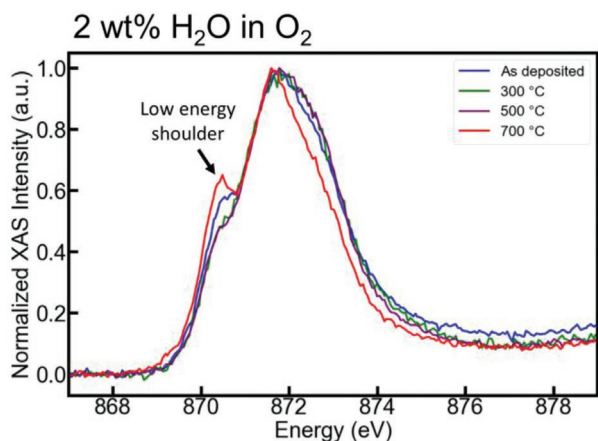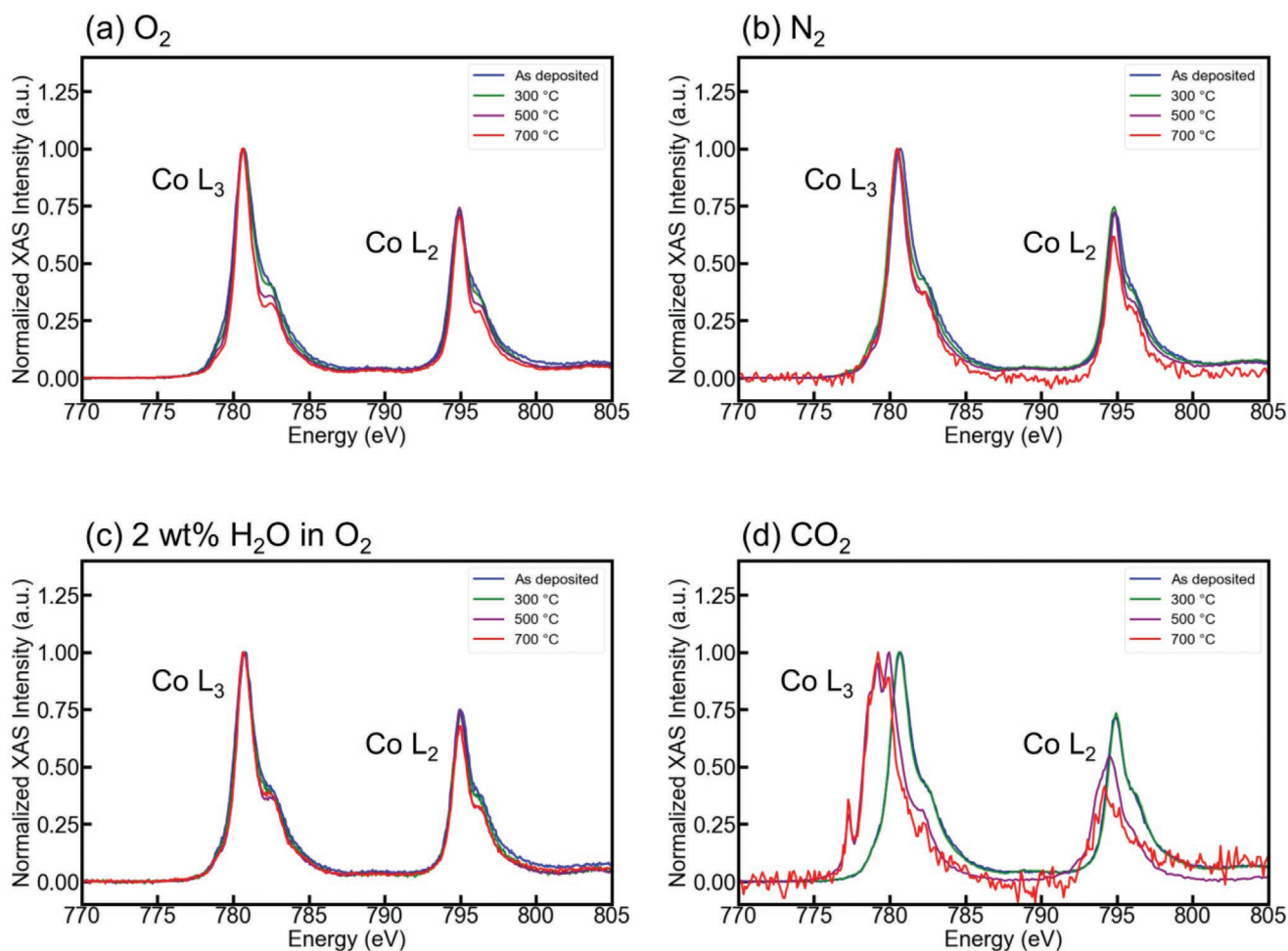

Figure 4. Ni L_2 X-ray absorption spectra measured by partial fluorescence yield mode for 100 nm NMC622|LLZO samples. Spectra for as deposited sample and sample annealed in humidified O_2 (2 wt% H_2O in O_2) for 4 h are shown. Intensities of peaks were normalized to 1.

temperature,[52,65] dehydration of hydrated NMC622 would also leave reduced phases.

Ni L_2-edge shape for samples annealed in CO_2 at 500 and 700 °C corresponded to Ni^{2+} (Figure 3d).[66,67] This is the decisive proof for secondary phase formation as NMC622 cannot consist of 100% Ni^{2+} regardless of Li concentration.

Figure 5 shows Co L-edge spectra. We normalized signals by the height of the Co L_3 edge. Annealing in pure O_2 did not cause oxidation state change of Co, as seen by the constant peak position of the L_3 and L_2 edges. Moreover, shoulder features of L_3 and L_2 got gradually sharper as annealing temperature increased, which indicates better ordering in the film with crystallinity improvement. Although we cannot easily resolve this from XRD, it is reasonable to expect an increased crystalline order in the NMC622 films with increasing temperature. Therefore, this result indicates that O_2 environment is the ideal sintering environment, as Co remains chemically stable during sintering, along with improved crystallinity of the NMC622 film.

Figure 5. Co L_3, Co L_2 X-ray absorption spectra measured by partial fluorescence yield (PFY) mode for 100 nm NMC622|LLZO samples. Spectra for as deposited sample and sample annealed in a) O_2, b) N_2, c) 2 wt% H_2O in O_2, and d) CO_2 for 4 h are shown. Intensities of peaks were normalized by Co L_3 edge.

Co was reduced after annealing in N_2, as seen by Co L-edge shift toward lower energy (Figure 5b). Co was also reduced at 700 °C in humidified O_2 (Figure 5c). Co L_3/L_2 intensity ratio increased at 700 °C, which indicated reduction of Co.[68] Reduction in N_2 environment came from oxygen loss, and reduction in humidified O_2 environment came from dehydration of the sample.

Annealing in CO_2 resulted in severe reduction of samples at 500 and 700 °C (Figure 5d). The shape of both spectra matched with octahedrally coordinated Co^{2+},[69,70] which was clearly different from spectral shape for Co^{3+} (low spin). This is a major evidence for phase decomposition since Co with +2 oxidation state does not exist in NMC622.

3.3. Structural Characterization of the Interface by X-Ray Diffraction

We performed XRD characterization to investigate whether crystalline secondary phases formed after annealing in each gas environment. **Figure 6**a–d shows 1D XRD plots obtained using Co anode.

Secondary phases did not form after annealing in O_2 (Figure 6a) and N_2 (Figure 6b). We observed peaks for LLZO (ICDD:01-084-6181), and small Li_2CO_3 (ICDD: 00-022-1141) peaks from all samples. Li_2CO_3 formed due to air exposure during sample transfer and XRD characterization. In order to identify the upper limit of temperature that gives rise to a chemically stable interface in pure O_2, we annealed the NMC622|LLZO sample in O_2 at 900 °C. La_2O_3 (ICDD: 00-005-0602) and $La_2Zr_2O_7$ (ICDD: 01-070-5602) formed at 900 °C (Figure S1, Supporting Information). Thus we can conclude that the annealing temperature should be lower than 900 °C in O_2 to avoid formation of secondary phases.

Intensity for Li_2CO_3 peaks were higher from samples annealed in humidified O_2 compared to O_2 and N_2 treated samples (Figure 6c). LiOH(s) could have formed during hydration of LLZO, which formed Li_2CO_3 during sample transport to the XRD by reacting with $CO_2(g)$ in air. Both of the reactions are thermodynamically favorable at 25 °C.[32] In addition, $La_2Zr_2O_7$ (ICDD: 01-070-5602) formed at 700 °C, potentially due to Li loss via LiOH(s) formation during annealing.
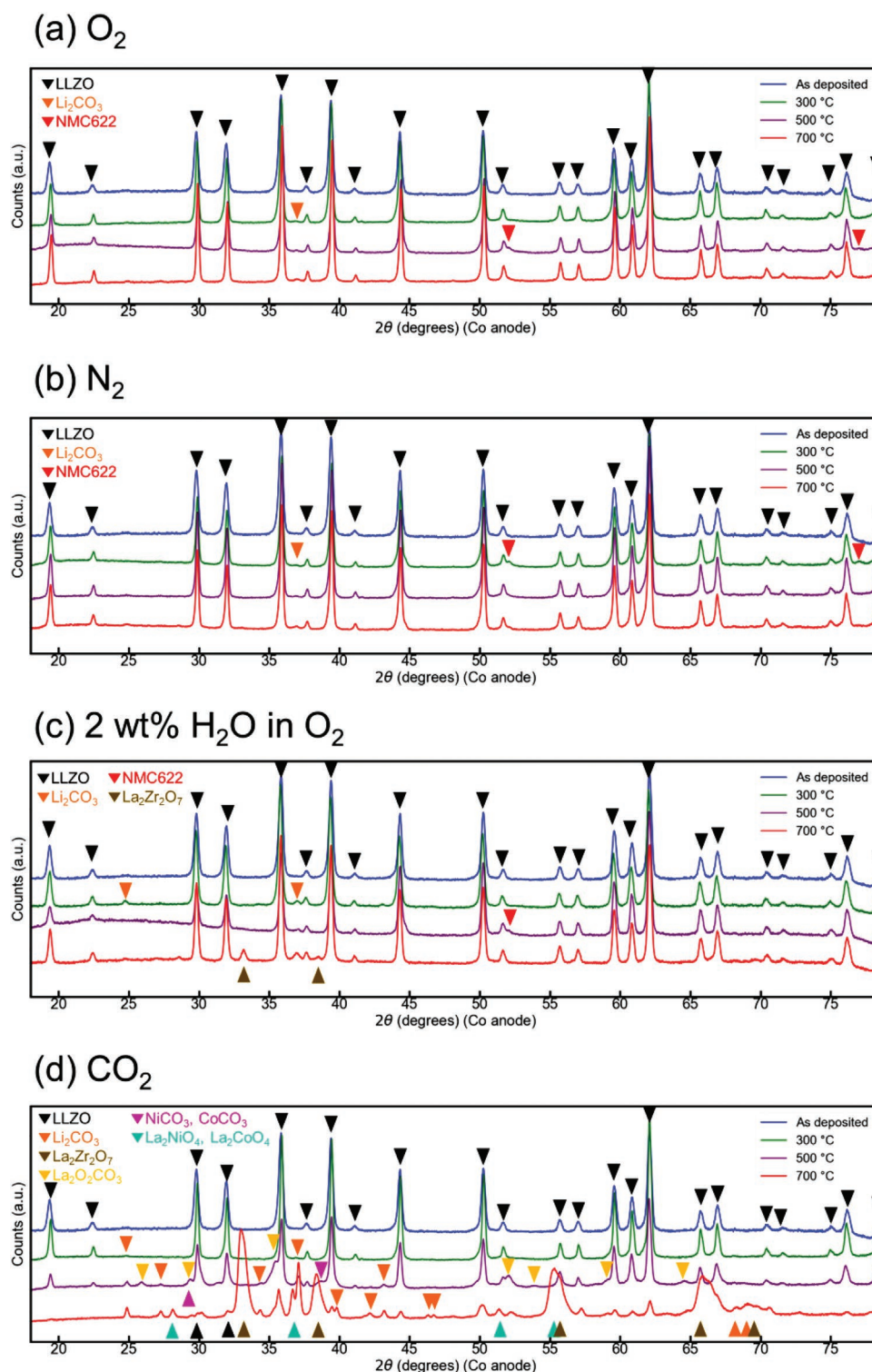
Figure 6. 1D XRD plots for 100 nm NMC622|LLZO samples. Plots for as deposited sample and samples annealed in a) O_2, b) N_2, c) 2 wt% H_2O in O_2, and d) CO_2 for 4 h are shown.

As for the CO_2 treated sample (Figure 6d), Li_2CO_3 formed at 300 °C, Li_2CO_3, $La_2O_2CO_3$, $NiCO_3$, and $CoCO_3$ formed at 500 °C, and Li_2CO_3, $La_2O_2CO_3$, $NiCO_3$, $CoCO_3$, La_2NiO_4, La_2CoO_4, and $La_2Zr_2O_7$ formed at 700 °C.

Formation of $NiCO_3$, $CoCO_3$, La_2NiO_4, and La_2CoO_4 is consistent with XAS analysis as they contain Ni^{2+} and Co^{2+}. XRD peak positions for samples annealed at 500 and 700 °C matched with $NiCO_3$ (ICDD:04-002-6999) (29.5° (40.5%), 38.6° (100%))

**ADVANCED
SCIENCE NEWS**
www.advancedsciencenews.com

**ADVANCED
ENERGY
MATERIALS**
www.advenergymat.de

Figure 7. Reaction products at NMC622|LLZO interfaces at different temperatures in each gas environment as deduced by XAS and XRD analysis in this work. Reaction product for annealing in air is from our previous work[30] and shown here for comparison.

interface as a function of gas and temperature environment. Findings from annealing in air are from our previous paper, which we show here for comparison. Red boxes indicate secondary phases formed in each experimental condition. In the case of humidified O_2 environment, LiOH that formed during annealing further degrades into Li_2CO_3 when the sample was exposed to air after the gas exposure experiment.

3.4. Implication of Heat Treatment in Each Gas Environment on Interfacial Resistance

We performed EIS on symmetric cells, Au|NMC622|LLZO|NMC622|Au, to evaluate the effect of annealing in each gas environment on cathode|electrolyte interfacial resistance. We repeated each experiment twice, and obtained the same trend. All EIS experiments were done at room temperature.

We used a circuit model consisting of $(R_{bulk}C_{bulk})(R_{interface1}CPE_{interface1})(CPE_{tail})(L)$ to analyze the impedance spectra from the as deposited sample (**Figure 8**) and the samples annealed in O_2 (**Figure 9**), N_2 (**Figure 10**), and humidified O_2 (**Figure 11**). We used different impedance ranges on the x-axes and y-axes for the figures to clearly show the semicircle corresponding to cathode|electrolyte interfacial resistance in all figures. Figures plotted with same x-axes and y-axes ranges are in Figures S2–S6, Supporting Information.

$(R_{bulk}C_{bulk})$ circuit element corresponds to capacitance of bulk LLZO pellet, and it appeared as a high frequency semicircle found at 2 MHz in all samples. C_{bulk} from samples were in the range of 20 to 60 pF. Considering the geometry of the sample, relative permittivity was in the range of 30–100, which was consistent with former EIS studies on LLZO pellets,[71,72]

and $CoCO_3$ (ICDD: 00-011-0692) (29.2° (40.0%), 38.1° (100%)). As for the sample annealed at 700 °C, we also assigned peaks for La_2NiO_4 (ICDD:04-014-8282) (28.0° (30.2%), 36.6° (100%), 51.2° (31.4%), and 55.2° (32.1%)) and La_2CoO_4 (ICDD: 04-013-8633) (27.9° (28.1%), 36.7° (100%), 51.3° (32.6%), and 54.9° (32.9%)).

La containing secondary phases without any transition metals formed as well. $La_2O_2CO_3$ (ICDD:00-037-0804) formed at 500 and 700 °C as seen by peaks at 35.4° (100%), 52.0° (75%), which are two strongest peaks of the phase. $La_2Zr_2O_7$ (ICDD: 01-070-5602) formed at 700 °C, showing clear XRD peaks at 33.3° (100%), 38.7° (29.9%), 55.9° (44.3%), and 66.7° (36.9%).

Figure 7 summarizes the experimental findings from XAS and XRD analysis on chemical stability of NMC622|LLZO

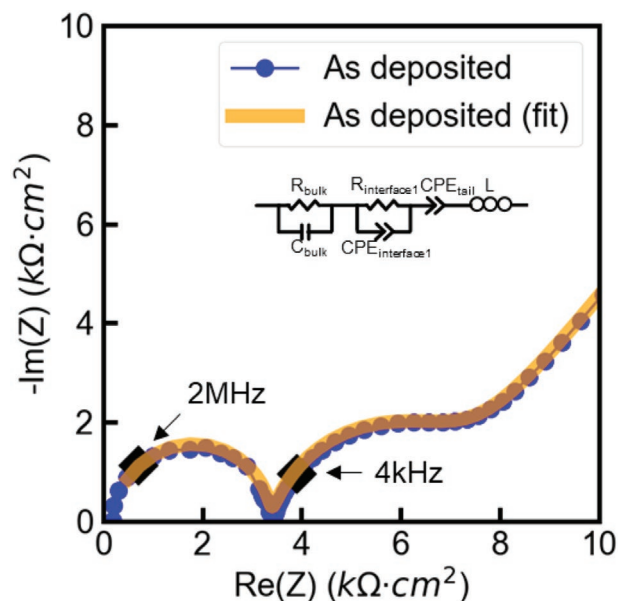**Figure 8.** Electrochemical impedance spectroscopy plot for Au|NMC622|LLZO|NMC622|Au symmetric cells with as deposited condition. (5 MHz–31.5 Hz): $R_{interface1}/2 = 1.52$ kΩ·cm² Frequency range for the data with impedance less than 10 kΩ cm² has been plotted.

ADVANCED
SCIENCE NEWS
www.advancedsciencenews.com

ADVANCED
ENERGY
MATERIALS
www.advenergymat.de

Figure 9. Electrochemical impedance spectroscopy plot for Au|NMC622|LLZO|NMC622|Au symmetric cells annealed in O_2 for 4 h. Frequency range for the data with impedance less than 10 k$\Omega\cdot$cm^2 has been plotted. Annealed at a) 300 °C (5 MHz–19.9 Hz): $R_{interface1}/2$ = 1.36 kΩ cm^2, b) 500 °C (3.97 MHz–3.15 Hz): $R_{interface1}/2$ = 0.29 kΩ cm^2, and c) 700 °C (5 MHz–19.9 Hz): $R_{interface1}/2$ = 0.13 k$\Omega\cdot$cm^2.

and our former work with the same sample design.[30] Inductance (L) originates from wiring of the experimental setup. CPE_{tail} describes behaviors of blocking electrodes at low frequency. These two circuit elements were used in previous EIS study on LLZO pellets,[71,72] and our own previous work on symmetric cells with same structure.[30] ($R_{interface1}CPE_{interface1}$) originates from capacitance at the cathode|electrolyte interface. Semicircles corresponding to this circuit element appeared at 4 kHz, which are consistent with our former works on similarly constructed symmetric cells (Au|LiCoO$_2$|LLZO|LiCoO$_2$|Au,[29] Au|NMC622|LLZO|NMC622|Au[30]). $CPE_{interface1}$ for the as-deposited sample and the samples annealed in O_2, N_2, and humidified O_2 were $\approx$10^{-7} F, which agrees with former findings from our group[29] and reported values for electrode|electrolyte interface.[73]

EIS for samples annealed in CO_2 was drastically different from other gas conditions (**Figure 12**). Three arcs are present in the spectrum from the sample annealed at 300 °C, so we have used two RC elements for the interface, ($R_{bulk}C_{bulk}$)

($R_{interface1}CPE_{interface1}$)($R_{interface2}CPE_{interface2}$)($CPE_{tail}$)($L$), for analysis. The second RC element that appears in the spectrum is likely due to formation of secondary phases as a result of interface reactions and degradation at 300 °C. In our previous study on NMC622|LLZO thermal degradation in air, such an additional arc appeared also from samples with interfacial degradation.[30] Total nominal resistance at the interface (($R_{interface1}$+ $R_{interface2}$)/2) equaled 9.01 k$\Omega\cdot$cm^2.

The arc for the cathode|electrolyte interfacial charge transfer capacitance did not appear from the sample annealed at 500 °C. This is consistent with the finding that the NMC622 cathode degraded into secondary phases containing Ni^{2+} and Co^{2+} as indicated by XAS (Figures 3d,5d) and XRD results (Figure 6d), so the interfacial charge transfer capacitance was lost. At 700 °C, the sample became both ionic and electronic insulator. Data points for the high frequency range followed an RC element behavior with a very high resistance, but quantification was not possible due to noise in data for the low frequency range. Noisy data originate from low current used for data acquisition, which
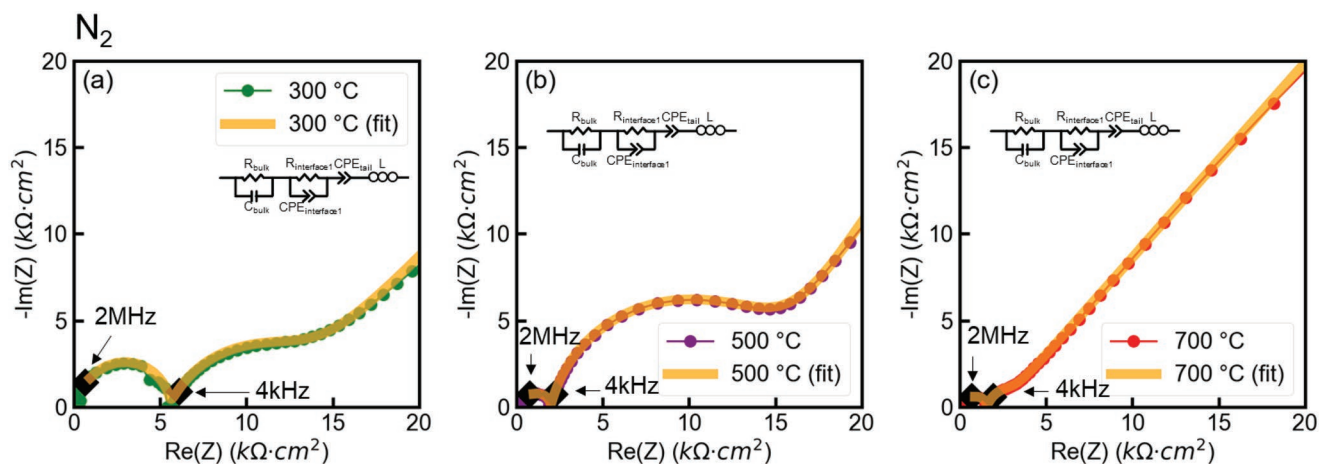

Figure 10. Electrochemical impedance spectroscopy plot for Au|NMC622|LLZO|NMC622|Au symmetric cells annealed in N_2 for 4 h. Frequency range for the data with impedance less than 20 kΩ cm^2 has been plotted. Annealed at a) 300 °C (5 MHz–6.29 Hz): $R_{interface1}/2$ = 3.34 kΩ cm^2, b) 500 °C (3.97 MHz–6.29 Hz): $R_{interface1}/2$ = 6.04 kΩ cm^2, and c) 700 °C (3.97 MHz–2.51 Hz): $R_{interface1}/2$ = 0.41 kΩ cm^2.

**ADVANCED
SCIENCE NEWS**

www.advancedsciencenews.com

**ADVANCED
ENERGY
MATERIALS**

www.advenergymat.de
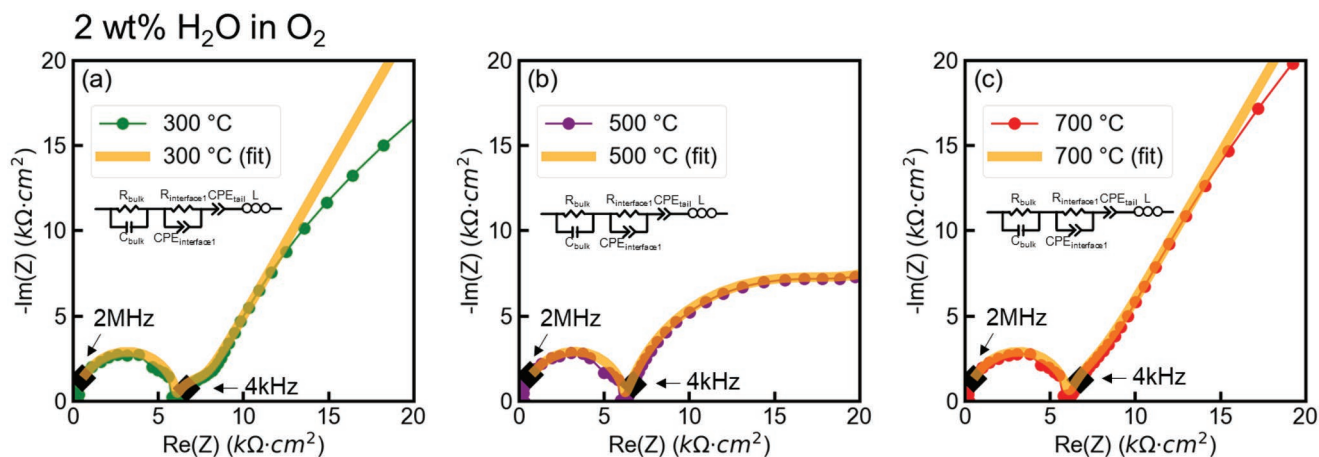
Figure 11. Electrochemical impedance spectroscopy plot for Au|NMC622|LLZO|NMC622|Au symmetric cells annealed in humidified O_2 (2 wt% H_2O in O_2) for 4 h. Frequency range for the data with impedance less than 20 kΩ cm² has been plotted. Annealed at a) 300 °C (5 MHz–15.8 Hz): $R_{interface1}/2 = 0.58$ kΩ·cm², b) 500 °C (3.97 MHz–50 Hz): $R_{interface1}/2 = 5.65$ kΩ·cm², and c) 700 °C (3.97 MHz–50 Hz): $R_{interface1}/2 = 0.35$ kΩ cm².

was due to high resistance. High resistance originates from formation of insulating secondary phases at 700 °C, which we have discussed above as part of the XRD analysis (Figure 6d). Intensities of XRD peaks from the LLZO phase were much weaker than those at other conditions, so significant amount of electrolyte phase decomposition also took place, consistent with the disappearance of the bulk Li-ion conduction arc in EIS.

Figure 13 shows ASR arising from the interface component of EIS, for the as deposited sample and the samples annealed in O_2, N_2, humidified O_2, CO_2, and air. ASR data for samples annealed in air are from our previous work.[30] We plotted the data here to compare the trend. We calculated ASR for a single cathode|electrolyte interface by $\frac{R_{interface1}}{2} \times Area$ for the as-deposited sample and the samples annealed in O_2, N_2, humidified O_2, and by $\frac{R_{interface1} + R_{interface2}}{2} \times Area$ for the sample annealed in CO_2. Division by 2 was due to the symmetric cell design, which had two equivalent NMC622|LLZO interfaces.

ASR gradually decreased as annealing temperature increased in pure O_2 environment. This confirmed that pure O_2 is the most promising condition for sintering the NMC622 and LLZO interface, since it decreased the ASR without any interfacial degradation up to 700 °C.

In contrast, ASR for samples annealed in N_2 increased up to 500 °C and decreased at 700 °C. ASR increase up to 500 °C came from interfacial degradation due to oxygen loss. ASR decrease at 700 °C was likely due to expedited sintering[74] in the presence of oxygen vacancies as seen by XAS in in NMC622. This led to improved bonding between NMC622 and LLZO.

ASR for samples annealed in humidified O_2 increased at 500 °C and decreased at 700 °C. This is because of hydration at 500 °C and dehydration at 700 °C, which we identified by XAS. Li^+/H^+ substitution during hydration leads to a contraction of the O-Li-O layer thickness in the layered oxide structure, and this increases the activation energy for Li diffusion.[52] This explains the ASR increase at 500 °C. Dehydration at 700 °C restored the Li^+ transport pathway and led to ASR decrease. We believe the
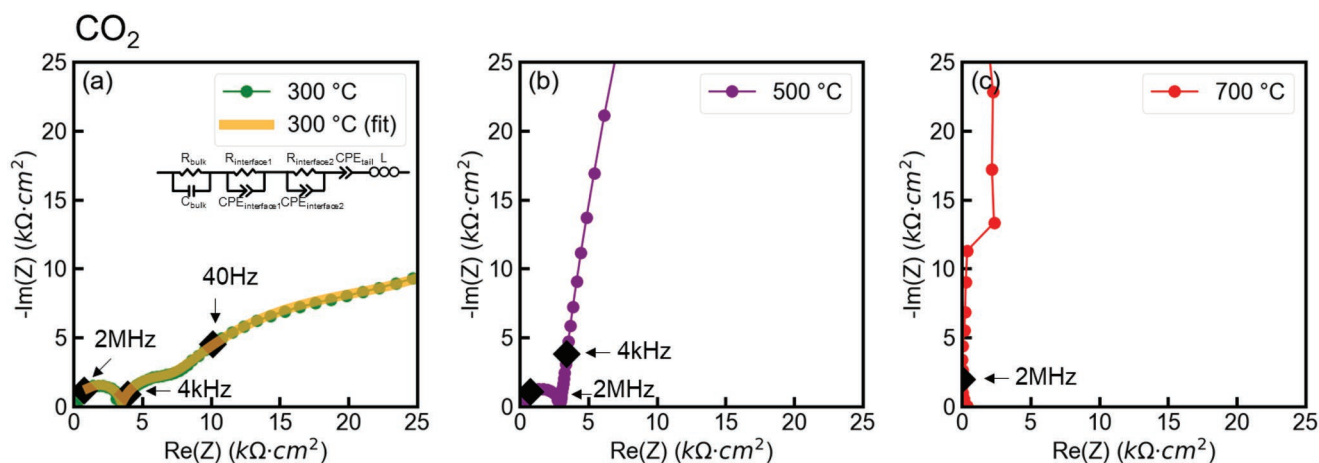
Figure 12. Electrochemical impedance spectroscopy plot for Au|NMC622|LLZO|NMC622|Au symmetric cells. Frequency range for the data with impedance less than 25 kΩ cm² has been plotted. Annealed at a) 300 °C (3.97 MHz–1.58 Hz): $(R_{interface1} + R_{interface2})/2 = 9.01$ kΩ·cm², b) 500 °C (3.97 MHz–0.63 kHz), and c) 700 °C (5 MHz–199 kHz) in CO_2 for 4 h.

2102741 (11 of 18)

**ADVANCED
SCIENCE NEWS**

www.advancedsciencenews.com

**ADVANCED
ENERGY
MATERIALS**

www.advenergymat.de
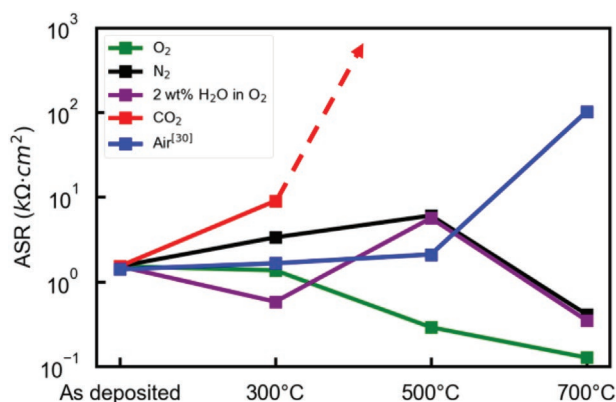
Figure 13. Area specific resistance (ASR) corresponding to single NMC622|LLZO interface. Data obtained from the as deposited sample and the samples annealed in O_2, N_2, humidified O_2 (2 wt% H_2O in O_2), CO_2, and air for 4 h are shown. Data for samples annealed in air are from our previous work,[30] and plotted here for comparison.

ASR decrease at 300 °C could arise from cold sintering in presence of humidity. Cold sintering uses a transient aqueous environment, the material surface dissolves into introduced H_2O, and the dissolved phases diffuse into pores and precipitates the solid phase.[75] It is considered a mediated dissolution-precipitation process, effectively decreasing the volume of pores and enabling sintering of particles. Therefore, the presence of controlled humidity in our experiments may have enabled further densification and sintering of the cathode layer and the cathode–electrolyte interface at low temperatures. While a lot yet has to be resolved about the mass transport at liquid–solid interfaces involved in cold sintering, this process can create a new opportunity to sinter ceramic electrolyte and cathode layers without thermally-driven reactions at the interface. Cold sintering on solid electrolyte[76] and cathode material[77] were shown to improve densification even at relatively low temperature (<300 °C). This can lead to a decreased ASR in our system as well.

Interfacial resistance increased steeply after annealing in CO_2. Notably, interfacial resistance became too high to measure when the annealing temperature was 500 and 700 °C. This fits with severe degradation at those temperatures demonstrated by XAS and XRD results. None of the phases in XRD characterization observed have known Li conductivity. Thus we conclude CO_2 environment is the most detrimental phase for sintering, leading to formation of insulating secondary phases.

While pure CO_2 is a lot more aggressive than the ppm-levels of CO_2 in air, the steep increase of interfacial resistance along with the formation of delithiated phases and Li_2CO_3 are consistent with our previous findings from annealing the NMC|LLZO in air.[30] After annealing at 700 °C in air, La(Ni,Co)O_3, $La_2Zr_2O_7$, and Li_2CO_3 formed and interfacial resistance at NMC622|LLZO interface increased by two orders of magnitude compared to as deposited state. While here in pure CO_2 we find more extensive, a wider range of degradation products, similarities of reaction pathway and interfacial resistance increase indicate that CO_2 was the key contributor of the interfacial degradation in air.

Lastly, we can also see variations of the bulk resistance of LLZO in Figures 9–11. This likely originates from the conduc-

tivity variation of LLZO pellets themselves, and is not related to annealing at different conditions. Conductivities of LLZO pellets differ in literature by two orders of magnitude even if they were prepared by nominally the same experimental procedure.[71] This can result in the different resistances of bulk LLZO in Figures 8–11. It is also possible that the LLZO bulk conductivity can vary by doping as a result of transition metal migration from NMC622 into LLZO during thermal treatment. However, doping of Ni and Co into LLZO decreases bulk ionic conductivity of LLZO.[78] This does not explain the EIS data in Figures 9,10, in which the bulk resistance of LLZO for samples annealed at higher temperatures (potentially more diffusion of Ni and Co into LLZO) is lower than the samples annealed at lower temperatures. Therefore, potential doping of LLZO from NMC622 during annealing is not the dominant reason for the variations in bulk resistance of LLZO in the annealing experiments.

3.5. Cycling Properties of the NMC622|LLZO Annealed in Pure O_2

We have electrochemically cycled the sample that was annealed at 500 °C in pure O_2. The NMC622|LLZO interface was chemically stable without secondary phase formation in this thermal condition as seen by the XAS and XRD results explained above. Interfacial charge transfer resistance at this condition was also lower than in the as-deposited sample, indicating improved interface sintering.

Figure 14 shows charge–discharge cycles for the Pt|NMC622|LLZO|Li cell. 1st charge capacity was 117 mAh g^{-1}, and 1st discharge capacity was 77 mAh g^{-1}, both comparable to an earlier report on NMC622|LLZO all solid battery with a Li_3BO_3 interlayer.[43] Irreversible capacity loss happened during the 1st cycle, as capacity for the 2nd charge dropped sharply to 61 mAh g^{-1}. Both the charge capacity and discharge capacity decreased gradually from 2nd to 10th cycle.

We performed differential capacity analysis to identify the voltages at which electrochemical reactions happen. **Figure 15** shows differential capacity curves for the 1st, 2nd, and 10th cycles. Three distinguishable peaks appeared in the differential capacity curve for the 1st charge at 3.7, 3.85, and 4.2 V. These
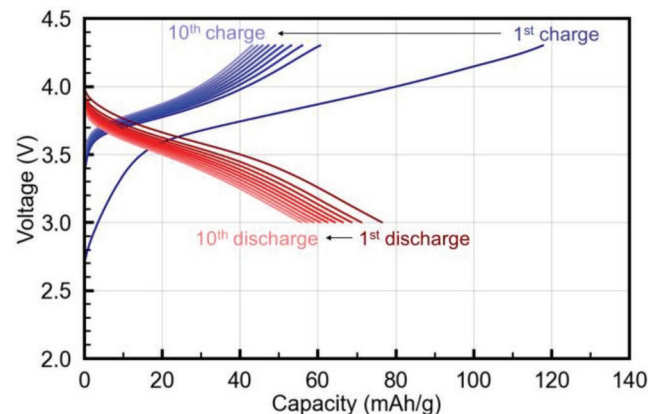
Figure 14. Charge and discharge cycles for the Pt|NMC622|LLZO|Li cell. 0.5 C current was used for cycling at 80 °C.
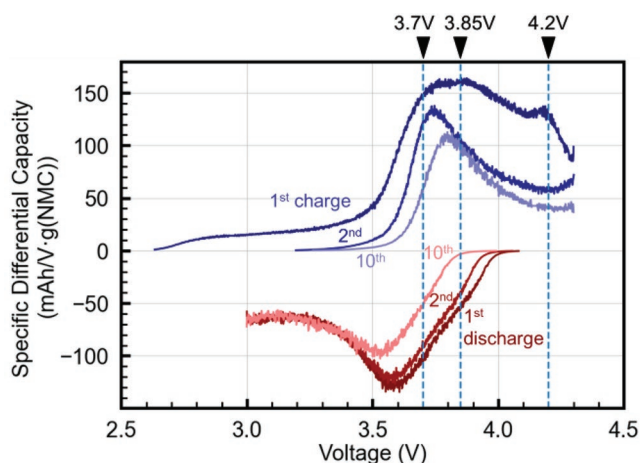
Figure 15. Differential capacity as a result of cycling the Pt|NMC622|LLZO|Li cell with ten cycles. The 1st, 2nd, and 10th cycles are shown. 0.5 C current was used for cycling at 80 °C.

correspond to the H1 (Hexagonal) → M (Monoclinic), M (Monoclinic) → H2 (Hexagonal), and H2 (Hexagonal) → H3 (Hexagonal) transitions of the NMC622 cathode, respectively.[79,80]

Only the features for H1 → M and M → H1 transitions appeared for all charge–discharge cycles. Moreover, peaks for H1 → M and M → H1 transitions shifted gradually with increasing cycle number, indicating an overpotential increase. Zhang et al. also observed peak shift during cycling of solid batteries based on $Li_{10}GeP_2S_{12}$, and attributed the phenomena to degradation at $LiCoO_2$|$Li_{10}GeP_2S_{12}$ interface.[81]

We attribute the sharp decrease in capacity and the increase in interfacial resistance after the first cycle to both electrochemical and mechanical instability at the NMC622|LLZO interface. Oxidation limit of LLZO according to density functional theory calculations is 2.91 V versus Li/Li+.[36] Secondary phase formation due to chemical reaction could have decreased capacity, similar to the case of solid state batteries with sulfide electrolyte ($Li_{10}GeP_2S_{12}$).[82] In addition, loss of contact between NMC622 and LLZO originating from cracks and delamination at the NMC622|LLZO interface could have also decreased capacity. Crack formation and delamination at the cathode|electrolyte interface and interfacial resistance increase after initial cycling were also found in other studies on NMC622|LLZO solid state batteries with interface coatings[43,83] and on NMC811|$Li_{10}SnP_2S_{12}$ solid state batteries.[84]

As the electrochemical performance of our best cell with the thin film cathode design, and the cells with composite cathodes made of LLZO and layered oxide cathode particles from literature[43,83] are consistent with each other, we can justify the usage of our cell as a model system to understand the thermally-induced interfacial degradation in NMC622|LLZO cells.

4. Discussion

We were able to isolate the potential contributions to degradation when LLZO and a layered transition metal oxide is co-sintered in air, by using gas components from air as pure gases in the annealing environment, specifically O_2, N_2, CO_2, and humidified O_2. As seen from the chemical, structural, and electrochemical data presented above, pure O_2 environment was ideal during annealing the NMC622|LLZO interface up to 700 °C, giving rise to a chemically stable interface with lower resistance. Secondary phases did not form after annealing in N_2, either, so it can be considered as an alternative potentially less expensive choice compared to pure O_2. In contrast, annealing in humidified environment and CO_2 environment led to the formation of secondary phases. Detrimental effect of CO_2 on interfacial degradation was the most severe. These experimental results of relative stability in different gas conditions are consistent with our Gibbs free energy analysis of reactions between the layered transition metal oxide cathode material and LLZO electrolyte.

1st charge capacity of the Pt|NMC622|LLZO|Li cell was 117 mAh g−1 and 1st discharge capacity was 77 mAh g−1 for the cell prepared by annealing the NMC622|LLZO interface at 500 °C in pure O_2. In addition, the cell was cyclable for at least ten more cycles afterward. Voltages for both the lithiation and delithiation of the cathode of this cell are consistent with layered oxide cathodes in the form of powders.[79,80] This indicates that annealing NMC622|LLZO in O_2 produces cathode–electrolyte interfaces with the appropriate and relevant electrochemical properties. In addition, it justifies that our chemical and structural results obtained on such thin film cathode|LLZO model system are applicable to solid state batteries.

Sintering in O_2 would cost more, in terms of both energy and materials, compared to sintering in air due to the production of O_2, but this increase would be very small compared to the total energy consumption for the solid-state cell preparation. Based on calculations of Troy et al. on energy demand for manufacturing Al|$LiCoO_2$|LLZO|Li|Cu pouch cell,[85] we estimate co-sintering in O_2 environment will increase the total energy demand for manufacturing by only a mere 0.0027% (see Experimental Section for details). In addition, given the relatively low cost of O_2 ($40 per ton),[86] we expect the increase in material and supply cost for sintering in O_2 environment would be negligible. Moreover, O_2 is already being used to synthesize layered oxide cathodes such as lithium manganese rich lithium nickel manganese cobalt oxide cathodes (LMR-NMC).[87] However, the more complicated system to keep operations safe in pure O_2 and to minimize O_2 loss can add to the cost of this approach. N_2 environment can be a more cost-effective alternative to pure O_2 environment. No secondary phases were detectable by XAS and XRD in NMC622|LLZO. In N_2, however, oxygen loss from NMC622 takes place at 700 °C according to XAS. Nevertheless, oxygen loss did not cause degradation of the cathode phase or its interface. Interfacial resistance decreased at 700 °C, and this is attributed to better sintering in the presence of oxygen vacancies.

In humidified O_2 environment, degradation driven by hydration took place at 500 °C and recovery due to dehydration at 700 °C. A γ-NiOOH-like local environment formed at 500 °C, which we justified by XAS and attributed to Li+/H+ exchange in the cathode by hydration. Annealing at 700 °C reversed the detrimental effect of humidity by dehydration. Therefore, heat treatment at sufficiently high temperature could restore the sample even after hydration. This finding is consistent with

ADVANCED
SCIENCE NEWS
www.advancedsciencenews.com

ADVANCED
ENERGY
MATERIALS
www.advenergymat.de

former studies on Li containing ceramics which are prone to Li^+/H^+ exchange in humidified environment. Protonated LLZO loses mass around 450 to 500 °C due to deprotonation in a form of H_2O evolution.[88–90] Deprotonation of $Li_{1-x}H_xNiO_2$ was also found at 200 to 220 °C and 300 to 320 °C by thermogravimetric analysis.[52]

CO_2 environment was the most detrimental to the NMC622|LLZO interface, leading to the formation of secondary phases at 500 and 700 °C. The presence of Li_2CO_3 and $La_2Zr_2O_7$ as a result of annealing in CO_2 matched with our previous findings in NMC622|LLZO when annealed in air.[30] Peak intensities of LLZO from the sample annealed at 700 °C was very low, indicating most of LLZO within the detection depth had degraded into secondary phases. In addition, carbonated species ($La_2O_2CO_3$, $NiCO_3$, and $CoCO_3$) and reduced species (La_2NiO_4, La_2CoO_4) were also found when the sample was annealed in CO_2. This severe degradation originates from higher P_{CO_2} and lower P_{O_2} in pure CO_2 compared to air. These found secondary phases are not Li-ion conductors. Li_2CO_3 has limited Li-ion conductivity (10^{-3} mS cm^{-1}) at room temperature, much lower compared to that in LLZO.[91] $La_2Zr_2O_7$ and Ruddelsden-popper phases are also not Li-ion conductors.[27,92] We do not expect carbonated species ($La_2O_2CO_3$, $NiCO_3$, and $CoCO_3$) to have good Li-ion conductivities since they do not have Li in their lattice nor cation vacancy channel for lithium ion transport. As a result, these insulating secondary phases block Li transfer at the interface, resulting in the very high resistances found by EIS (Figure 12).

These findings justify our claim that Li_2CO_3 formation by reaction with ambient CO_2 is the deciding factor for the thermal interfacial degradation when the cathode(NMC622, LCO)-LLZO interface is sintered in air.[29,30] This experimental finding is in accordance with the Gibbs free energy analysis, which predicted spontaneous reaction between cathode and electrolyte even with partial pressure of CO_2 in air (4.12×10^{-4} atm for 412 ppm concentration[93]) at 300 to 700 °C (Figure 1).

The degradation reactions nucleate at the interface between the ceramic cathode and the ceramic electrolyte. In order to be sensitive to this process initiating at the interface, we have used thin film ($\leq$100 nm) cathode layers, so that we could capture the onset of the reactions even if only a small volume is affected. Because we are working with thin cathode layers, once the interface reactions nucleate and propagate, it looks as if we are transforming the bulk of the cathode layer, but this is because we are working with thin films. This is different from conventional cell design in which cathode particles with diameter larger than 1 μm are used.[40] For example in our prior work with LCO|LLZO, we have shown that 5–20 nm thickness from the interface is affected by these reactions at 300 °C, and about 100 nm at 500 °C.[29] Given the small volume and the disordered nature of these reacted interface zones, it is impossible to capture them with powder XRD at their onset conditions. Our approach combining thin-films with spectroscopy targets that, and captures the chemical and structural changes nucleating at the interface and propagating from the interface after they onset. This process indeed relates to the cathode–electrolyte interface reactions if powder cathode particles were used on an LLZO, but this does not necessarily mean the entire bulk of the cathode particles would have reacted in that more conventional geometry.

As a result, pure O_2 gas condition was ideal, with good interface stability and decrease of interface resistance up to 700 °C. NMC622|LLZO annealed at 700 °C in O_2 had the lowest ASR, 130 $\Omega\cdot cm^2$. This value is comparable to the lowest ASRs obtained at LiCoO$_2$|LLZO interfaces with coated interlayers;[94] for example 230 $\Omega\cdot cm^2$ with Li_3BO_3 interlayer,[39] 101 $\Omega\cdot cm^2$ with $Li_2CO_3 + Li_{2.3}C_{0.7}B_{0.3}O_3$ interlayer,[40] 150 $\Omega\cdot cm^2$ with Nb interlayer,[41] and 53.5 $\Omega\cdot cm^2$ with Nb_2O_5 interlayer.[42] In this work, by removing CO_2 from the gas environment during sintering, we succeeded in obtaining comparably low ASRs but without the need for an interlayer. This is an advantage, because the introduction of the interlayer coatings into the battery cell also introduces additional, elaborate, and costly thin-film processing steps in the fabrication of the battery. In order to be competitive with liquid batteries whose ASR is $\approx$22 $\Omega\cdot cm^2$,[95] we need to lower the ASR further. We expect the NMC622|LLZO interface ASR could be lowered further, for example by a fast firing technique at high temperature for a short time with high ramp rate,[96] to expedite and enhance densification at the interface.

Although we have not done experiments in dry air and synthetic air, we can predict the outcome based on our findings in this paper. Dry air or synthetic air can be other potential gas environment for annealing and bonding the NMC622|LLZO interface. As for dry air, we expect interfacial degradation since dry air still has CO_2, and the Gibbs free energy for the reaction was negative (spontaneous) with CO_2 partial pressure (of 4.12×10^{-4} atm for 412 ppm concentration[93]) in air. On the other hand, for synthetic air (made of pure O_2 and pure N_2) we do not expect interfacial degradations, since the environment is CO_2-free and the Gibbs free energy for the reaction was positive (non-spontaneous) and secondary phase did not form in both O_2 and N_2.

We also note that the degradation mechanism in CO_2 and the way to mitigate it on the LLZO-cathode interface is different from that on the LLZO-Li anode interface. On the LLZO-Li metal anode interface, CO_2 reacts with LLZO and forms Li_2CO_3, and this substantially degrades physical wetting and contact area of Li metal on LLZO, thus increases the interface resistance.[32,97] Physically removing that Li_2CO_3 prior to pressing the Li metal anode layer onto the ceramic electrolyte circumvents that issue.[32] What we find on the cathode side is very different. The degradation during synthesis of the cathode–electrolyte interface in air or in CO_2 is rather due to the formation of Li-deficient secondary phases, such as $La_2Zr_2O_7$ and perovskite-related oxides (e.g., La(Ni,Co)O$_3$), as a result of Li-loss in the form of Li_2CO_3, and not by loss of physical contact between LLZO and the oxide cathode. Therefore, one has to avoid formation of Li-deficient secondary phases. This can be done by avoiding CO_2 in the environment, and this approach reduces the interface resistance to lowest values reported in literature where elaborate coatings had to be used. We believe this is an important insight to guide how to synthesize cathode–electrolyte material interfaces in the best way.

5. Conclusion

The goal of this work was to isolate and identify the key contributors to degradation when LLZO and a layered

transition metal oxide are co-sintered in air. For that, we have used gas components from air as pure gases in the annealing environment of NMC622|LLZO, specifically O_2, N_2, CO_2, and humidified O_2 at 300 to 700 °C. Findings from our thermodynamic predictions (Gibbs free energy analysis of reactions), chemical and structural characterization (XAS and XRD), and electrochemical analysis (EIS) correlate well with each other. Annealing in pure O_2 gas has given the best result. The interface remained stable at up to 700 °C while interfacial resistance at room temperature decreased from 1500 to 130 $\Omega \cdot cm^2$. This is comparable to the lowest interface ASR values obtained by using protective interlayer coatings between LLZO and layered transition metal cathodes; but here without the additional step of an interface coating. Capacities and potentials of charging/discharging plateaus for the Pt|NMC622|LLZO|Li cell prepared by annealing the NMC622|LLZO in pure O_2 matched well with previous studies on NMC622. The interface also remained free of secondary phases when annealed in N_2. However, oxygen loss took place at 700 °C. In humidified O_2, NMC622 was hydrated at up to 500 °C and dehydrated at 700 °C, consistent with the calculated Gibbs free energy of reactions. Therefore, if a completely dry environment is not possible, using sufficiently high sintering temperature can minimize or avoid the detrimental effect of humidity. Annealing in CO_2 was the worst condition, and caused the formation of insulating secondary phases that block and diminish the charge transfer capability. Removing $CO_2(g)$ from the sintering gas environment is important for the successful co-sintering of LLZO and layered transition metal oxide cathode materials without interfacial degradation. Co-sintering in pure O_2 environment gives the best result in terms of both interfacial chemical stability and interfacial resistance.

6. Experimental Section

LLZO Synthesis and Pellet Preparation: Al doped LLZOpellets were prepared in a two-step process. The first step was to make LLZO powder by solid-state reaction. The precursors (Li_2CO_3, La_2O_3, ZrO_2, and Al_2O_3) were mixed in a mortar for 30 min. Al:Li:La:Zr molar ratio in the mixture was 0.24:6.9:3:2. 10% excess Li was used to compensate for Li loss during the high temperature treatment. The mixture was sintered in an alumina crucible at 900 °C for 12 h in air. After the heat treatment, the product was grinded in a mortar for 30 min to make fine powder. The second step was to make pellets from the powder. The powder was pressed in a 10 mm diameter pressing die to make pellets. The pellets were sintered in an MgO crucible at 1160 °C for 15 h in air. The pellets were covered with LLZO powder during sintering to compensate for Li evaporation. The sintered pellets were polished using 600, 800, 1000, and 1200 grit paper in sequence.

NMC622 and Gold Film Deposition: RF sputtering was used to prepare NMC622 and Gold thin film. Targets were 2 inch in diameter. Deposition condition was 100 W power and 3 mTorr pressure at room temperature. Ar:O_2 ratio was 3:1 for NMC622 deposition. Pure Ar was used for Au deposition. NMC622 target with 10% excess Li was used to compensate for Li loss during sputtering. The sample stage was rotated during deposition for uniform deposition.

Gibbs Free Energy Calculation: The temperature and pressure dependence of Gibbs free energy was calculated as following.

First, the formula for $C_p(T)$ for each phase was obtained. Data from NIST-JANAF thermochemical tables were used to obtain $C_p(T)$ for Li_2CO_3, Li_2O, Li_2O_2, LiOH, O_2, CO_2, and H_2O.[98] $C_p(T)$ for LLZO[99] and $LiCoO_2$[100] were given by respective former works. As for $La_2Zr_2O_7$[101] and $LaCoO_3$,[102] given C_p for discrete temperatures were fitted experimentally to the following function.

$$C_p(T) = A + BT + CT^2 + DT^3 + \frac{E}{T^2} \tag{5}$$

Second, $H°(T,1\,bar)$ and $S°(T,1\,bar)$ for each phase were calculated by using standard formation enthalpy ($H_f°(298.15\,K, 1\,bar)$), standard entropy ($S°(298.15\,K, 1\,bar)$), and $C_p(T)$. Data from NIST-JANAF thermochemical tables were used to acquire standard formation enthalpy and standard entropy for Li_2CO_3, Li_2O, Li_2O_2, LiOH, O_2, CO_2, and H_2O.[98] Standard formation enthalpy and standard entropy for LLZO,[99] $LiCoO_2$,[103] $La_2Zr_2O_7$,[101] and $LaCoO_3$[102,104] are given from corresponding works. Terms for $C_p(T)$ of elements weren't considered when calculating $H°(T,1bar)$ since they cancel out in the next step.

$$H°(T,1\,bar) = H_f°(298.15\,K, 1\,bar) + \int_{298.15\,K}^{T} C_p(T_1)dT_1 \tag{6}$$

$$S°(T,1\,bar) = S°(298.15\,K, 1\,bar) + \int_{298.15\,K}^{T} \frac{C_p(T_1)}{T_1}dT_1 \tag{7}$$

Third, $\Delta H°(T,1\,bar)$ and $\Delta S°(T,1\,bar)$ for the proposed reaction were calculated by using $H°(T,1\,bar)$ and $S°(T,1\,bar)$ found for each phase in the previous step.

Finally, $\Delta G(T, P_{gas})$ for the proposed reaction was calculated by using $\Delta H°(T,1\,bar)$, $\Delta S°(T,1\,bar)$ found in previous step and considering pressure dependence. Since $|(\frac{\partial G}{\partial P})_T|$ for the gas phase was much bigger than the solid or liquid phase, the pressure dependence of gas phase was only considered.

$$\Delta G(T,P) = \Delta H°(T,1\,bar) - T\Delta S°(T,1\,bar) + \sum n_{gas}RT\ln\frac{P_{gas}}{P°} \tag{8}$$

$$P° = 1\,bar \tag{9}$$

Bruker GADDS X-Ray Diffraction: Co anode (wavelength: 1.79 Å) was used for XRD measurement. The sample stage was rotated at a constant speed ($\approx60°\,min^{-1}$) during data acquisition to avoid effect of preferential orientation of grains. The Bragg–Brentano geometry was used for XRD measurement. A 0.5 mm pinhole incident-beam collimator was used, and the sample-to-detector distance was kept at 159 mm. Three 2D XRD images were obtained for each sample, and the image was processed to 1D XRD plot in Figure 6. **Table 1** summarizes experimental conditions used to obtain 2D XRD images. Each image contained 2048 × 2048 pixels, and needed 1 h data acquisition time.

Soft X-Ray Absorption Spectroscopy: O K-edge, Ni $L_{2,3}$-edge, La $M_{4,5}$-edge, and Co $L_{2,3}$-edge spectra were measured at the 23-ID-2 (IOS) beamline, National Synchrotron Light Source II (NSLS-II) in partial fluorescence yield mode using a Vortex EM silicon drift detector. The data were analyzed using Athena software.[105]

Electrochemical Impedance Spectroscopy: EIS data were collected using PARSTAT 4000, with 100 mV AC amplitude at room temperature. The data were processed using ZView software (Scribner).

Table 1. Center angle, start angle, and end angle for each 2D XRD image used to make 1D XRD plot.

Center angle (2θ)	30.00°	45.00°	60.00°
Start angle (2θ)	11.20°	26.20°	41.21°
End angle (2θ)	51.24°	65.21°	79.41°

**ADVANCED
SCIENCE NEWS**

www.advancedsciencenews.com

**ADVANCED
ENERGY
MATERIALS**

www.advenergymat.de

Electrochemical Cycling: The cell was cycled between 3.0 and 4.3 V with 0.5 C current assuming 187 mAh g^{-1} theoretical capacity at 80 °C using Autolab PGSTAT204. Noise on the differential capacity curve was reduced by following the approaches of Thompson et al.[106] First, the differential capacity at each voltage point was calculated using the following approximation.

$$\left(\frac{dQ}{dV}\right)_i = \frac{Q_i - Q_{i-1}}{V_i - V_{i-1}} \tag{10}$$

Second, only data points with a voltage difference higher than 0.0007 V were used for analysis so that the denominator was large enough. Third, the Savitzky–Golay filter(order: 3, window length: 9) was applied on the obtained differential capacity curve.

Energy and Cost Assessment for Co-Sintering in O$_2$ Environment: Troy et al. found that the energy needed to make a 5 cm by 5 cm Al|LiCoO$_2$|LLZO|Li|Cu pouch cell with 43.75 mAh capacity was 156.4 MJ per cell.[85] The calculation included the energy demand for material synthesis, tape casting, co-sintering, and cell assembly. The extra energy needed for co-sintering in O$_2$ environment was calculated using the following approach. First, the total amount of oxygen required for co-sintering in oxygen environment was estimated by assuming 100 sccm flow rate with 1 h sintering time. The sintering time was chosen by considering works on fabricating LLZO-based all solid batteries using tape casting.[107–109] The total weight of O$_2$ needed for co-sintering is given by the following formula.

$$1.31\times 10^{-3}\ \text{g cm}^{-3}\left(density\ of\ \text{O}_2\right)\times 100\ \text{cm}^3\ \text{min}^{-1}\times 60\ \text{min} = 7.86\ \text{g} \tag{11}$$

Second, the energy needed to produce O$_2$ was calculated. The energy needed for oxygen separation from air by cryogenic method was 150 kWh per ton O$_2$ (540 MJ per ton O$_2$)[110] Therefore, the total energy needed for producing oxygen for co-sintering is as following.

$$7.86\ \text{g}\times 1\ ton\ per\ 10^6\ \text{g}\times 540\ MJ\ ton^{-1} = 4.24\ kJ \tag{12}$$

The additional energy consumption needed for the preparation of oxygen for co-sintering increased the total energy needed for cell preparation by 0.0027%.

For solid batteries based on LLZO solid electrolyte, the price of LLZO overwhelms the prices of other constituents. The current market price of Ampcera LLZO sold by MSE Supplies was $675 per 100 g. The price was at least two orders of magnitude higher than cathode or anode materials when compared for the same weight.[111] The total weight of LLZO used for making Al|LiCoO$_2$|LLZO|Li|Cu pouch cell by Troy et al. was 10 g, which would cost $67.5. The price of oxygen prepared by cryogenic method was $40 per ton.[86] The price for 7.86 g O$_2$, which was needed for co-sintering was $0.0003. This was 4×10^{-6} of the price of LLZO. This was a negligible contribution to the materials and supplies cost of battery manufacturing.

Supporting Information

Supporting Information is available from the Wiley Online Library or from the author.

Conflict of Interest

The authors declare no conflict of interest.

Author Contributions

Y.K. synthesized materials and prepared samples. Y.K., I.W., and A.H. performed the XAS measurements. Y.K. did thermodynamic calculations, and conducted XRD, EIS, and electrochemical cycling. Y.K. and B.Y. analyzed all the data, and wrote the manuscript. B.Y. designed and supervised the work.

Data Availability Statement

The data that support the findings of this study are available from the corresponding author upon reasonable request.

[1] T. Famprikis, P. Canepa, J. A. Dawson, M. S. Islam, C. Masquelier, *Nat. Mater.* **2019**, *18*, 1278.

[2] Q. Liu, Z. Geng, C. Han, Y. Fu, S. Li, Y. He, F. Kang, B. Li, *J. Power Sources* **2018**, *389*, 120.

[3] T. Thompson, S. Yu, L. Williams, R. D. Schmidt, R. Garcia-Mendez, J. Wolfenstine, J. L. Allen, E. Kioupakis, D. J. Siegel, J. Sakamoto, *ACS Energy Lett.* **2017**, *2*, 462.

[4] Y. Zhu, X. He, Y. Mo, *ACS Appl. Mater. Interfaces* **2015**, *7*, 23685.

[5] J.-M. Tarascon, M. Armand, *Nature* **2001**, *414*, 359.

[6] A. C. Luntz, J. Voss, K. Reuter, *J. Phys. Chem. Lett.* **2015**, *6*, 4599.

[7] A. Banerjee, X. Wang, C. Fang, E. A. Wu, Y. S. Meng, *Chem. Rev.* **2020**, *120*, 6878.

[8] Y. Xiao, Y. Wang, S.-H. Bo, J. C. Kim, L. J. Miara, G. Ceder, *Nat. Rev. Mater.* **2020**, *5*, 105.

[9] Y. Ren, Y. Shen, Y. Lin, C.-W. Nan, *Electrochem. Commun.* **2015**, *57*, 27.

[10] E. J. Cheng, A. Sharafi, J. Sakamoto, *Electrochim. Acta* **2017**, *223*, 85.

[11] C.-L. Tsai, V. Roddatis, C. V. Chandran, Q. Ma, S. Uhlenbruck, M. Bram, P. Heitjans, O. Guillon, *ACS Appl. Mater. Interfaces* **2016**, *8*, 10617.

[12] H. Duan, Y.-X. Yin, Y. Shi, P.-F. Wang, X.-D. Zhang, C.-P. Yang, J.-L. Shi, R. Wen, Y.-G. Guo, L.-J. Wan, *J. Am. Chem. Soc.* **2018**, *140*, 82.

[13] B. Wu, S. Wang, J. Lochala, D. Desrochers, B. Liu, W. Zhang, J. Yang, J. Xiao, *Energy Environ. Sci.* **2018**, *11*, 1803.

[14] H. Huo, Y. Chen, R. Li, N. Zhao, J. Luo, J. G. Pereira da Silva, R. Mücke, P. Kaghazchi, X. Guo, X. Sun, *Energy Environ. Sci.* **2020**, *13*, 127.

[15] X. Han, Y. Gong, K. (Kelvin) Fu, X. He, G. T. Hitz, J. Dai, A. Pearse, B. Liu, H. Wang, G. Rubloff, Y. Mo, V. Thangadurai, E. D. Wachsman, L. Hu, *Nat. Mater.* **2017**, *16*, 572.

[16] J. Fu, P. Yu, N. Zhang, G. Ren, S. Zheng, W. Huang, X. Long, H. Li, X. Liu, *Energy Environ. Sci.* **2019**, *12*, 1404.

[17] A. Sharafi, E. Kazyak, A. L. Davis, S. Yu, T. Thompson, D. J. Siegel, N. P. Dasgupta, J. Sakamoto, *Chem. Mater.* **2017**, *29*, 7961.

[18] K. Nie, Y. Hong, J. Qiu, Q. Li, X. Yu, H. Li, L. Chen, *Front. Chem.* **2018**, *6*, 616.

[19] H.-D. Lim, J.-H. Park, H.-J. Shin, J. Jeong, J. T. Kim, K.-W. Nam, H.-G. Jung, K. Y. Chung, *Energy Storage Mater.* **2020**, *25*, 224.

[20] J. Xu, E. Hu, D. Nordlund, A. Mehta, S. N. Ehrlich, X.-Q. Yang, W. Tong, *ACS Appl. Mater. Interfaces* **2016**, *8*, 31677.

[21] D. Wang, C. Zhu, Y. Fu, X. Sun, Y. Yang, *Adv. Energy Mater.* **2020**, *10*, 2001318.

[22] K. J. Kim, M. Balaish, M. Wadaguchi, L. Kong, J. L. M. Rupp, *Adv. Energy Mater.* **2021**, *11*, 2002689.

[23] X. Yu, A. Manthiram, *Energy Environ. Sci.* **2018**, *11*, 527.

[24] Y. Xiao, L. J. Miara, Y. Wang, G. Ceder, *Joule* **2019**, *3*, 1252.

[25] K. Park, B.-C. Yu, J.-W. Jung, Y. Li, W. Zhou, H. Gao, S. Son, J. B. Goodenough, *Chem. Mater.* **2016**, *28*, 8051.

[26] Y. Ren, T. Liu, Y. Shen, Y. Lin, C.-W. Nan, *J. Materiomics* **2016**, *2*, 256.

[27] K. H. Kim, Y. Iriyama, K. Yamamoto, S. Kumazaki, T. Asaka, K. Tanabe, C. A. J. Fisher, T. Hirayama, R. Murugan, Z. Ogumi, *J. Power Sources* **2011**, *196*, 764.

[28] N. Zhang, X. Long, Z. Wang, P. Yu, F. Han, J. Fu, G. Ren, Y. Wu, S. Zheng, W. Huang, C. Wang, H. Li, X. Liu, *ACS Appl. Energy Mater.* **2018**, *1*, 5968.

[29] G. Vardar, W. J. Bowman, Q. Lu, J. Wang, R. J. Chater, A. Aguadero, R. Seibert, J. Terry, A. Hunt, I. Waluyo, D. D. Fong, A. Jarry, E. J. Crumlin, S. L. Hellstrom, Y.-M. Chiang, B. Yildiz, *Chem. Mater.* **2018**, *30*, 6259.

[30] Y. Kim, D. Kim, R. Bliem, G. Vardar, I. Waluyo, A. Hunt, J. T. Wright, J. P. Katsoudas, B. Yildiz, *Chem. Mater.* **2020**, *32*, 9531.

[31] W. D. Richards, L. J. Miara, Y. Wang, J. C. Kim, G. Ceder, *Chem. Mater.* **2016**, *28*, 266.

[32] A. Sharafi, S. Yu, M. Naguib, M. Lee, C. Ma, H. M. Meyer, J. Nanda, M. Chi, D. J. Siegel, J. Sakamoto, *J. Mater. Chem. A* **2017**, *5*, 13475.

[33] W. Xia, B. Xu, H. Duan, X. Tang, Y. Guo, H. Kang, H. Li, H. Liu, *J. Am. Ceram. Soc.* **2017**, *100*, 2832.

[34] H. S. Liu, Z. R. Zhang, Z. L. Gong, Y. Yang, *Electrochem. Solid-State Lett.* **2004**, *7*, A190.

[35] H. Liu, Y. Yang, J. Zhang, *J. Power Sources* **2006**, *162*, 644.

[36] F. Han, Y. Zhu, X. He, Y. Mo, C. Wang, *Adv. Energy Mater.* **2016**, *6*, 1501590.

[37] S.-M. Bak, E. Hu, Y. Zhou, X. Yu, S. D. Senanayake, S.-J. Cho, K.-B. Kim, K. Y. Chung, X.-Q. Yang, K.-W. Nam, *ACS Appl. Mater. Interfaces* **2014**, *6*, 22594.

[38] Y. Zhu, X. He, Y. Mo, *J. Mater. Chem. A* **2016**, *4*, 3253.

[39] S. Ohta, S. Komagata, J. Seki, T. Saeki, T. Morishita, T. Asaoka, *J. Power Sources* **2013**, *238*, 53.

[40] F. Han, J. Yue, C. Chen, N. Zhao, X. Fan, Z. Ma, T. Gao, F. Wang, X. Guo, C. Wang, *Joule* **2018**, *2*, 497.

[41] T. Kato, T. Hamanaka, K. Yamamoto, T. Hirayama, F. Sagane, M. Motoyama, Y. Iriyama, *J. Power Sources* **2014**, *260*, 292.

[42] J. Sastre, X. Chen, A. Aribia, A. N. Tiwari, Y. E. Romanyuk, *ACS Appl. Mater. Interfaces* **2020**, *12*, 36196.

[43] D. Wang, Q. Sun, J. Luo, J. Liang, Y. Sun, R. Li, K. Adair, L. Zhang, R. Yang, S. Lu, H. Huang, X. Sun, *ACS Appl. Mater. Interfaces* **2019**, *11*, 4954.

[44] B. Wang, J. B. Bates, F. X. Hart, B. C. Sales, R. A. Zuhr, J. D. Robertson, *J. Electrochem. Soc.* **1996**, *143*, 3203.

[45] X. Zhu, Z. Guo, G. Du, P. Zhang, H. Liu, *Surf. Coat. Technol.* **2010**, *204*, 1710.

[46] H.-S. Kim, Y. Oh, K. H. Kang, J. H. Kim, J. Kim, C. S. Yoon, *ACS Appl. Mater. Interfaces* **2017**, *9*, 16063.

[47] J. B. Bates, N. J. Dudney, B. J. Neudecker, F. X. Hart, H. P. Jun, S. A. Hackney, *J. Electrochem. Soc.* **2000**, *147*, 59.

[48] F. M. F. de Groot, M. Grioni, J. C. Fuggle, J. Ghijsen, G. A. Sawatzky, H. Petersen, *Phys. Rev. B* **1989**, *40*, 5715.

[49] J. Suntivich, W. T. Hong, Y.-L. Lee, J. M. Rondinelli, W. Yang, J. B. Goodenough, B. Dabrowski, J. W. Freeland, Y. Shao-Horn, *J. Phys. Chem. C* **2014**, *118*, 1856.

[50] E.-J. Guo, Y. Liu, C. Sohn, R. D. Desautels, A. Herklotz, Z. Liao, J. Nichols, J. W. Freeland, M. R. Fitzsimmons, H. N. Lee, *Adv. Mater.* **2018**, *30*, 1705904.

[51] Y. Zhong, J. Dai, X. Xu, C. Su, Z. Shao, *ChemElectroChem* **2020**, *7*, 4949.

[52] T. Toma, R. Maezono, K. Hongo, *ACS Appl. Energy Mater.* **2020**, *3*, 4078.

[53] I. A. Shkrob, J. A. Gilbert, P. J. Phillips, R. Klie, R. T. Haasch, J. Bareño, D. P. Abraham, *J. Electrochem. Soc.* **2017**, *164*, A1489.

[54] R. Moshtev, P. Zlatilova, S. Vasilev, I. Bakalova, A. Kozawa, *J. Power Sources* **1999**, *81*, 434.

[55] D. Pritzl, T. Teufl, A. T. S. Freiberg, B. Strehle, J. Sicklinger, H. Sommer, P. Hartmann, H. A. Gasteiger, *J. Electrochem. Soc.* **2019**, *166*, A4056.

[56] S. Jeong, J. Kim, J. Mun, *J. Electrochem. Soc.* **2019**, *166*, A5038.

[57] N. Li, D. K. Bediako, R. G. Hadt, D. Hayes, T. J. Kempa, F. von Cube, D. C. Bell, L. X. Chen, D. G. Nocera, *Proc. Natl. Acad. Sci. USA* **2017**, *114*, 1486.

[58] R. Qiao, Y.-D. Chuang, S. Yan, W. Yang, *PLoS One* **2012**, *7*, e49182.

[59] J. Stöhr, *NEXAFS Spectroscopy*, Springer, Berlin **2011**.

[60] F. M. F. de Groot, Z. W. Hu, M. F. Lopez, G. Kaindl, F. Guillot, M. Tronc, *J. Chem. Phys.* **1994**, *101*, 6570.

[61] F. May, M. Tischer, D. Arvanitis, M. Russo, J. H. Dunn, H. Henneken, H. Wende, R. Chauvistré, N. Mårtensson, K. Baberschke, *Phys. Rev. B* **1996**, *53*, 1076.

[62] M.-S. Kim, T.-S. Hwang, K.-B. Kim, *J. Electrochem. Soc.* **1997**, *144*, 1537.

[63] F. Lin, I. M. Markus, D. Nordlund, T.-C. Weng, M. D. Asta, H. L. Xin, M. M. Doeff, *Nat. Commun.* **2014**, *5*, 3529.

[64] C. Tian, D. Nordlund, H. L. Xin, Y. Xu, Y. Liu, D. Sokaras, F. Lin, M. M. Doeff, *J. Electrochem. Soc.* **2018**, *165*, A696.

[65] J. Pan, Y. Sun, P. Wan, Z. Wang, X. Liu, *Electrochem. Commun.* **2005**, *7*, 857.

[66] H. Ikeno, I. Tanaka, Y. Koyama, T. Mizoguchi, K. Ogasawara, *Phys. Rev. B* **2005**, *72*, 075123.

[67] L. A. Montoro, M. Abbate, E. C. Almeida, J. M. Rosolen, *Chem. Phys. Lett.* **1999**, *309*, 14.

[68] S. Hwang, S. M. Kim, S.-M. Bak, S. Y. Kim, B.-W. Cho, K. Y. Chung, J. Y. Lee, E. A. Stach, W. Chang, *Chem. Mater.* **2015**, *27*, 3927.

[69] F. M. F. de Groot, M. Abbate, J. van Elp, G. A. Sawatzky, Y. J. Ma, C. T. Chen, F. Sette, *J. Phys.: Condens. Matter* **1993**, *5*, 2277.

[70] J. van Elp, J. L. Wieland, H. Eskes, P. Kuiper, G. A. Sawatzky, F. M. F. de Groot, T. S. Turner, *Phys. Rev. B* **1991**, *44*, 6090.

[71] A. Wachter-Welzl, J. Kirowitz, R. Wagner, S. Smetaczek, G. C. Brunauer, M. Bonta, D. Rettenwander, S. Taibl, A. Limbeck, G. Amthauer, J. Fleig, *Solid State Ionics* **2018**, *319*, 203.

[72] A. Wachter-Welzl, R. Wagner, D. Rettenwander, S. Taibl, G. Amthauer, J. Fleig, *J. Electroceram.* **2017**, *38*, 176.

[73] J. T. S. Irvine, D. C. Sinclair, A. R. West, *Adv. Mater.* **1990**, *2*, 132.

[74] I. Reimanis, H.-J. Kleebe, *J. Am. Ceram. Soc.* **2009**, *92*, 1472.

[75] J. Guo, H. Guo, A. L. Baker, M. T. Lanagan, E. R. Kupp, G. L. Messing, C. A. Randall, *Angew. Chem., Int. Ed.* **2016**, *55*, 11457.

**ADVANCED
SCIENCE NEWS**

www.advancedsciencenews.com

**ADVANCED
ENERGY
MATERIALS**

www.advenergymat.de

[76] S. S. Berbano, J. Guo, H. Guo, M. T. Lanagan, C. A. Randall, *J. Am. Ceram. Soc.* **2017**, *100*, 2123.

[77] J.-H. Seo, K. Verlinde, J. Guo, D. S. B. Heidary, R. Rajagopalan, T. E. Mallouk, C. A. Randall, *Scr. Mater.* **2018**, *146*, 267.

[78] X. Cheng, J. Huang, W. Qiang, B. Huang, *Ceram. Int.* **2020**, *46*, 3731.

[79] H.-J. Noh, S. Youn, C. S. Yoon, Y.-K. Sun, *J. Power Sources* **2013**, *233*, 121.

[80] R. Jung, M. Metzger, F. Maglia, C. Stinner, H. A. Gasteiger, *J. Electrochem. Soc.* **2017**, *164*, A1361.

[81] W. Zhang, F. H. Richter, S. P. Culver, T. Leichtweiss, J. G. Lozano, C. Dietrich, P. G. Bruce, W. G. Zeier, J. Janek, *ACS Appl. Mater. Interfaces* **2018**, *10*, 22226.

[82] C. Wang, S. Hwang, M. Jiang, J. Liang, Y. Sun, K. Adair, M. Zheng, S. Mukherjee, X. Li, R. Li, H. Huang, S. Zhao, L. Zhang, S. Lu, J. Wang, C. V. Singh, D. Su, X. Sun, *Adv. Energy Mater.* **2021**, *11*, 2100210.

[83] T. Liu, Y. Zhang, R. Chen, S.-X. Zhao, Y. Lin, C.-W. Nan, Y. Shen, *Electrochem. Commun.* **2017**, *79*, 1.

[84] X. Liu, B. Zheng, J. Zhao, W. Zhao, Z. Liang, Y. Su, C. Xie, K. Zhou, Y. Xiang, J. Zhu, H. Wang, G. Zhong, Z. Gong, J. Huang, Y. Yang, *Adv. Energy Mater.* **2021**, *11*, 2003583.

[85] S. Troy, A. Schreiber, T. Reppert, H.-G. Gehrke, M. Finsterbusch, S. Uhlenbruck, P. Stenzel, *Appl. Energy* **2016**, *169*, 757.

[86] G. B. Tuson, H. Kobayashi, M. J. Campbell, *Oxygen Enriched Combustion System Performance Study. Phase 2: 100 Percent Oxygen Enriched Combustion in Regenerative Glass Melters, Final Report*, University of North Texas Libraries, USA **1994**.

[87] J. B. Dunn, L. Gaines, J. C. Kelly, C. James, K. G. Gallagher, *Energy Environ. Sci.* **2015**, *8*, 158.

[88] G. Larraz, A. Orera, M. L. Sanjuán, *J. Mater. Chem. A* **2013**, *1*, 11419.

[89] Z. F. Yow, Y. L. Oh, W. Gu, R. P. Rao, S. Adams, *Solid State Ionics* **2016**, *292*, 122.

[90] C. Liu, K. Rui, C. Shen, M. E. Badding, G. Zhang, Z. Wen, *J. Power Sources* **2015**, *282*, 286.

[91] M. Ebrahiminia, J. Hooper, D. Bedrov, *Crystals* **2018**, *8*, 473.

[92] Y. Chen, E. Rangasamy, C. R. dela Cruz, C. Liang, K. An, *J. Mater. Chem. A* **2015**, *3*, 22868.

[93] Y. Cui, B. A. Schubert, A. H. Jahren, *Geology* **2020**, *48*, 888.

[94] S. Xu, R. M. Jacobs, H. M. Nguyen, S. Hao, M. Mahanthappa, C. Wolverton, D. Morgan, *J. Mater. Chem. A* **2015**, *3*, 17248.

[95] A. Kim, S. Woo, M. Kang, H. Park, B. Kang, *Front. Chem.* **2020**, *8*, 468.

[96] S.-J. L. (Suk-J. L.) Kang, *Sintering : Densification, Grain Growth, and Microstructure*, Elsevier Butterworth-Heinemann, Amsterdam **2005**.

[97] L. Cheng, E. J. Crumlin, W. Chen, R. Qiao, H. Hou, S. F. Lux, V. Zorba, R. Russo, R. Kostecki, Z. Liu, K. Persson, W. Yang, J. Cabana, T. Richardson, G. Chen, M. Doeff, *Phys. Chem. Chem. Phys.* **2014**, *16*, 18294.

[98] M. W. Chase, NIST-JANAF Themochemical Tables, 4th ed. Maryland **1998**.

[99] E. A. Il'ina, A. A. Raskovalov, O. G. Reznitskikh, *J. Chem. Thermodyn.* **2019**, *128*, 68.

[100] P. Gotcu-Freis, D. M. Cupid, M. Rohde, H. J. Seifert, *J. Chem. Thermodyn.* **2015**, *84*, 118.

[101] M. Bolech, E. H. P. Cordfunke, A. C. G. Van Genderen, R. R. Van Der Laan, F. J. J. G. Janssen, J. C. Van Miltenburg, *J. Phys. Chem. Solids* **1997**, *58*, 433.

[102] S. Stølen, F. Grønvold, H. Brinks, T. Atake, H. Mori, *J. Chem. Thermodyn.* **1998**, *30*, 365.

[103] M. Wang, *Solid State Ionics* **2004**, *166*, 167.

[104] J. Cheng, A. Navrotsky, X.-D. Zhou, H. U. Anderson, *J. Mater. Res.* **2005**, *20*, 191.

[105] B. Ravel, M. Newville, *J. Synchrotron Radiat.* **2005**, *12*, 537.

[106] N. Thompson, T. Cohen, S. Alamdari, C.-W. Hsu, G. Williamson, D. Beck, V. Holmberg, *J. Open Source Softw.* **2020**, *5*, 2624.

[107] T. Liu, Y. Zhang, X. Zhang, L. Wang, S.-X. Zhao, Y.-H. Lin, Y. Shen, J. Luo, L. Li, C.-W. Nan, *J. Mater. Chem. A* **2017**, *6*, 4649.

[108] E. Yi, H. Shen, S. Heywood, J. Alvarado, D. Y. Parkinson, G. Chen, S. W. Sofie, M. M. Doeff, *ACS Appl. Energy Mater.* **2020**, *3*, 170.

[109] G. T. Hitz, D. W. McOwen, L. Zhang, Z. Ma, Z. Fu, Y. Wen, Y. Gong, J. Dai, T. R. Hamann, L. Hu, E. D. Wachsman, *Mater. Today* **2019**, *22*, 50.

[110] T. Banaszkiewicz, M. Chorowski, W. Gizicki, *Energy Procedia* **2014**, *51*, 127.

[111] E. J. Berg, C. Villevieille, D. Streich, S. Trabesinger, P. Novák, *J. Electrochem. Soc.* **2015**, *162*, A2468.